Ocean Modelling 149 (2020) 101611

Contents lists available at ScienceDirect

Ocean Modelling

journal homepage: www.elsevier.com/locate/ocemod

The wake of a three-dimensional underwater obstacle: Effect of bottom boundary conditions

Pranav Puthan [a], Masoud Jalali [a], Jose Luis Ortiz-Tarin [a], Karu Chongsiripinyo [b], Geno Pawlak [a], Sutanu Sarkar [a,*]

[a] University of California San Diego, La Jolla, CA 92093, USA
[b] Chulalongkorn University, Bangkok 10330, Thailand

ARTICLE INFO

Keywords:
Lee vortices
Turbulent wakes
Internal waves
Vorticity generation
Boundary conditions

ABSTRACT

Three-dimensional (3D) obstacles on the bottom are common sites for the generation of vortices, internal waves and turbulence by ocean currents. Turbulence-resolving simulations are conducted for stratified flow past a conical hill, a canonical example of 3D obstacles. Motivated by the use of slip boundary condition (BC) and drag-law (effectively partial slip) BC in the literature on geophysical wakes, we examine the sensitivity of the flow to BCs on the obstacle surface and the flat bottom. Four BC types are examined for a non-rotating wake created by a steady current impinging on a conical obstacle, with a detailed comparison being performed between two cases, namely **NOSL** (no-slip BC used at all solid boundaries) and **SL** (slip BC used at all solid boundaries). The other two cases are as follows: **Hybrid**, undertaken with slip at the flat bottom and no-slip at the obstacle boundaries, and case **DL** wherein a quadratic drag-law BC is adopted on all solid boundaries. The no-slip BC allows the formation of a boundary layer which separates and sheds vorticity into the wake. Significant changes occur in the structure of the lee vortices and wake when the BC is changed. For instance, bottom wall friction in the no-slip case suppresses unsteadiness of flow separation leading to a steady attached lee vortex. In contrast, when the bottom wall has a slip BC (the **SL** and **Hybrid** cases) or has partial slip (**DL** case), unsteady separation leads to a vortex street in the near wake and the enhancement of turbulence. The recirculation region is shorter and the wake recovery is substantially faster in the case of slip or partial-slip BC. In the lee of the obstacle, turbulent kinetic energy (TKE) for case **NOSL** is concentrated in a shear layer between the recirculating wake and the free stream, while TKE is bottom-intensified in the other three cases. **DL** is the appropriate BC for high-Re wakes where the boundary layer cannot be resolved. The sources of lee vorticity are also examined in this study for each choice of BC. The sloping sides lead to horizontal gradients of density at the obstacle, which create vorticity through baroclinic torque. Independent of the type of BC, the baroclinic torque dominates. Vortex stretch and tilt are also substantial. An additional unstratified free-slip case (**SL-UN**) is simulated and the wake is found to be thin without large wake vortices. Thus, stratification is necessary for the formation of coherent lee vortices of the type seen in geophysical wakes.

1. Introduction

The role of bottom topography in ocean dynamics has received increasing attention in recent years. The momentum transported by topographic internal waves acts as drag on the impinging flow, and the energy converted from the flow to internal waves acts as a source for both remote and local turbulent mixing. Along with internal waves, wakes are generated as the flow separates at three-dimensional (3D) steep, multiscale bathymetry, e.g. at Luzon Strait (Zheng et al., 2008; Pinkel et al., 2012; Buijsman et al., 2014). Separated flow and wake eddies in stratified water, for example, at the headlands of Three Tree Point (Pawlak et al., 2003; Canals et al., 2008) and Palau (MacKinnon et al., 2019) lead to form drag and, additionally, to turbulent dissipation and mixing. Stratification exerts significant dynamic control in these examples and in the model problem simulated here, unlike the more studied configuration of island wakes in shallow, well-mixed water. The role of wake vortices and attendant flow variability in flow past submerged topography has received less attention than internal waves, motivating the present study of a canonical problem of stratified flow past a conical hill with a focus on wake dynamics.

With the advent of computing power and improved simulation techniques, our ability to model wakes of flow past topography has advanced. Wakes of islands and seamounts have been simulated using ocean circulation models with early efforts by Beckmann and Haidvogel (1997) and Coutis and Middleton (2002) and more recent

* Corresponding author.
E-mail address: sarkar@ucsd.edu (S. Sarkar).

https://doi.org/10.1016/j.ocemod.2020.101611
Received 9 November 2019; Received in revised form 12 March 2020; Accepted 18 March 2020
Available online 26 March 2020
1463-5003/

work by Dong et al. (2007), Liu and Chang (2018) and Perfect et al. (2018). Flow separation and eddy formation off coastal topography has been examined for the California Undercurrent (Molemaker et al., 2015), the Gulf Stream (Gula et al., 2015), and for tidally modulated currents past Three Tree Point in the context of form drag (Warner and MacCready, 2014). Notably, submesoscale eddies with large vertical vorticity (relative to the inertial frequency) are injected into the flow. Furthermore, abyssal-ocean measurements at rough topography reveal strong boundary currents and elevated turbulent dissipation rates at bottom mixed layers (Polzin et al., 2014; Ruan et al., 2017; Garabato et al., 2019). The increasing resolution of ocean models also points to the importance of topographic features, e.g., enhanced tracer mixing as the Antarctic Circumpolar Current (ACC) passes through the Drake Passage (Mashayek et al., 2017) and enhanced submesoscale vortices as the ACC negotiates the Kerguelen Plateau in the South Indian Ocean (Rosso et al., 2015).

Consider a current of characteristic speed U_0 in a stratified background with buoyancy frequency N and Coriolis frequency f. As the current flows past an obstacle of horizontal length scale D and height h, a flow is established with dynamics governed by the following non-dimensional parameters: (1) Reynolds number (Re_D) defined as $U_0 D/\nu$ where ν is the viscosity, (2) topographic Froude number (Fr_h) defined as U_0/Nh, (3) topographic Rossby number (Ro) defined as U_0/fD, and (4) topographic slope h/D. The value of Fr_h is quite variable in deep water. For example, in the Southern Ocean, a current with $U_0 = 0.1$ ms^{-1} that flows over a hill of 200 m height in backgrounds with $N = 10^{-2}$–10^{-3} s^{-1} has $Fr_h = 0.05$–0.5, e.g. Nikurashin and Ferrari (2010). At $Fr_h = O(1)$, most of the fluid impinging on the obstacle is able to go over it and lee waves are generated. In the regime of $Fr_h < 1$, some of the upstream fluid is blocked from going over the obstacle and there are nonlinear hydraulic effects associated with blocking of flow at depths below a distance of $> O(U_0/N)$ from the crest (Baines, 1995). For 3D obstacles, the flow can instead go around the obstacle and its subsequent separation leads to lee vortices as found in laboratory experiments (Hunt and Snyder, 1980; Vosper et al., 1999).

In the present work, we consider a low Froude number of $Fr_h = 0.2$ where predominant horizontal flow is anticipated, along with a relatively steep slope of $h/D = 0.3$, which accentuates flow separation. Since Fr_h is not $\ll 1$, some of the oncoming fluid can go over the obstacle to generate internal waves. At near-equatorial locations, the importance of rotation diminishes. This scenario favors the generation of cyclonic and anticylonic eddies of nearly equal strength (Hasegawa et al., 2004). While several numerical studies of ocean wakes have focused extensively on the $Ro \ll 1$ regime, topographic wakes which belong to $Ro > O(1)$ have received less attention. Strong currents have been observed to separate in the lee of islands (Kimura et al., 1994; Hasegawa et al., 2004; Chang et al., 2019) and mountains (Chopra and Hubert, 1964; Grubisic et al., 2015). When currents encounter small obstacles (say $D = 500$ m), the topographic Rossby number can be as large as 10 (assuming inertial frequency at 15° N). Our study examines a model oceanic wake problem in this regime and rotation effects are excluded in this paper so as to focus on stratification effects in the absence of rotation.

Since our objective is to examine the flow in a model that resolves the boundary layer and the turbulence, a moderate Reynolds number of $Re_D = 15{,}000$ is chosen. This simulation model has been validated and used to examine stratified flow past a sphere (Pal et al., 2016, 2017; Chongsiripinyo and Sarkar, 2017).

Previous studies of atmospheric lee vortices in mountain wakes are relevant. Baroclinic generation, namely, the production of horizontal vorticity by baroclinic torque and its subsequent tilt towards the vertical, appears to be the favored mechanism for lee vortices rather than the vorticity injected by boundary layer separation. This mechanism was proposed by Smolarkiewicz and Rotunno (1988), prompted by their simulation of flow past a bell-shaped hill. Their model, which used a slip BC on all solid boundaries (therefore, no boundary layer), exhibited an attached lee vortex when Fr_h was decreased below ~0.5. The flow pattern was similar to that in laboratory experiments at similar Fr_h by Hunt and Snyder (1980). Subsequent work, e.g., Rotunno et al. (1998) and Epifanio and Rotunno (2005) has further developed this explanation by analysis of vorticity and potential vorticity (PV) balances. Alternate mechanisms for lee vortices in the case of slip BC have been proposed, e.g., streamline curvature of the boundary flow (Smith, 1989) and dissipative production of PV (Schar and Durran, 1996). No-slip BC has been employed by Ding and Street (2002) and their $Fr_h = 0.2$ simulation conducted at $Re_D = 730$ exhibits a steady attached vortex pair in the lee with little turbulence. Unlike the quasi-steady lee vortex found in several numerical models of the atmospheric hill wake, Schar and Durran (1996) and Vosper (2000) report an unsteady vortex street. Laboratory experiments of stratified flow past obstacles (Hunt and Snyder, 1980; Vosper et al., 1999) report lee vortices at Fr_h sufficiently below 1, but the cutoff value of Fr_h varies and is likely sensitive to Re_D, obstacle shape and freestream disturbances.

Similar to the previous numerical studies of a cylindrical island (Dong et al., 2007) and a conical seamount (Perfect et al., 2018), the present work is an idealized model. There are crucial differences too: (1) a hill with negligible rotation influence is considered here instead of large topography with $Ro < O(1)$, and (2) our numerical model is a non-hydrostatic turbulence-resolving LES in contrast to a hydrostatic ROMS model with parameterized turbulent eddy viscosity. The effective Reynolds number ranges up to 6400 in Dong et al. (2007) and is approximately 2000 in Perfect et al. (2018).

The literature review shows that stratified oceanic flows in a regime with both internal waves and some upstream blocking and, additionally, at high Rossby numbers have received less attention. In both atmospheric and oceanic applications, different types of BCs have been used and there is some disagreement among studies with respect to the formation and unsteadiness of lee vortices. We are thus motivated in the present study to examine the sensitivity of a non-rotating wake to various BCs with parameters as described by Table 2. The use of high-resolution LES also provides an opportunity to quantitatively study lee vortices including the wake vorticity balance in the presence of unsteady, dissipative motions of turbulence.

The problem is formulated in Section 2 where the governing equations, numerical model and simulation parameters are described. Section 3 is a discussion of how BCs impact several aspects of the flow including separation, the recirculation region and its unsteadiness, wake defect velocity and wake turbulence. The influence of BCs on vortex dynamics is discussed in Section 4, where the role of baroclinicity in the formation of lee vortices is also assessed. The paper concludes with a summary of the results and conclusions in Section 5.

2. Problem formulation

2.1. Governing equations

The 3D non-hydrostatic flow is modeled by the Navier–Stokes equations under the Boussinesq approximation. The equations for conservation of mass, momentum and density in a high Rossby number ($Ro \gg 1$) regime, are represented below in tensor notation:

$$\frac{\partial u_i}{\partial x_i} = 0, \tag{1}$$

$$\frac{\partial u_i}{\partial t} + u_j \frac{\partial u_i}{\partial x_j} = -\frac{1}{\rho_0}\frac{\mathrm{d}p^*}{\mathrm{d}x_i} - \frac{g\rho^*}{\rho_0}\delta_{i3} + \frac{\partial \tau_{ij}}{\partial x_j}, \tag{2}$$

$$\frac{\partial \rho}{\partial t} + u_j \frac{\partial \rho}{\partial x_j} = \frac{\partial \chi_j}{\partial x_j}. \tag{3}$$

The density field is decomposed as:

$$\rho = \rho_0 + \rho_{bg}(z) + \rho^*(x, y, z, t), \tag{4}$$

Table 1
Notation used in the model formulation and analysis of results.

x_i	= Position vector (x, y, z)
t	= Time
u_i	= Velocity vector (u, v, w)
(u, v, w)	= Streamwise, spanwise and vertical velocity components
(x^*, y^*, z^*)	= $(x/D, y/D, z/h)$
t^*	= tU/D
$\omega_i = \mathcal{E}_{ijk}\frac{\partial u_k}{\partial x_j}$	= Vorticity vector $(\omega_x, \omega_y, \omega_z)$
$\omega_i\omega_i$	= Enstrophy
$(\omega_x, \omega_y, \omega_z)$	= Streamwise, spanwise and vertical components of the vorticity vector
$\mathbf{n}, \mathbf{t_1}, \mathbf{t_2}$	= Wall normal vector and two mutually orthogonal tangent vectors
$\rho_{bg}(z)$, ρ_0	= Background density profile and reference density (resp.)
ρ, ρ^*	= Density and density deviation
$b = -g\rho^*/\rho_0$	= Buoyancy
$N = \sqrt{\frac{-g}{\rho_0}\frac{\mathrm{d}\rho}{\mathrm{d}z}}$	= Brunt–Väisäla frequency
p^*	= Pressure deviation from hydrostatic
g	= Gravitational acceleration
ν	= Kinematic viscosity
κ	= Thermal diffusivity
τ_{ij}	= Stress tensor
χ_i	= Density flux vector
$S_{ij} = \frac{1}{2}\left(\frac{\partial u_i}{\partial x_j} + \frac{\partial u_j}{\partial x_i}\right)$	= Rate of strain tensor
ν_{sgs}	= Subgrid scale eddy viscosity
κ_{sgs}	= Subgrid scale eddy diffusivity
$\overline{A}$	= LES filter applied to A
Δ	= LES filter length
C_s	= Smagorinsky coefficient

where ρ_{bg} is a linear function of z, leading to a constant N in the simulations. The large eddy simulation (LES) technique is employed to model the effect of unresolved scales of the flow. Thus, $\boldsymbol{\tau}_{ij}$ and χ_j include the contribution from both molecular viscosity and the subgrid-scale stress. The symbols used here are defined in Table 1.

2.2. Simulated Cases

The setup of the problem is illustrated in Fig. 1. The flow is initialized with uniform velocity, $\mathbf{u} = (U_0, 0, 0)$, which also serves as the inlet BC. At solid boundaries, the velocity vectors can be decomposed as u_n, u_{t_1} and u_{t_2}, where u_n is the velocity normal to the wall and u_{t_1}&u_{t_2} are the wall-tangential velocities. The BCs are varied among cases. In particular, the solid boundaries are either assigned as no-slip walls or slip walls:

$$\text{No-slip wall } (S = 0): \quad u_n = 0, \quad u_{t_1} = 0, \quad u_{t_2} = 0. \tag{5}$$

$$\text{Impermeable slip wall } (S = 1): \quad u_n = 0, \quad (\boldsymbol{\tau}\cdot\mathbf{n})\cdot\mathbf{t_1} = 0, \quad (\boldsymbol{\tau}\cdot\mathbf{n})\cdot\mathbf{t_2} = 0. \tag{6}$$

In the above equations, S is a parameter used to distinguish between a slip wall (where $S = 1$) and a no-slip wall ($S = 0$) as shown in Eq. (6). The no-slip bottom boundary is the physically accurate BC. Thus, when $S = 0$, a boundary layer (BL) develops upstream, which grows in thickness as the flow approaches the hill. The early development of the BL is visible in the velocity profile plotted at $x^* = x/D = -2.4$ in Fig. 2(a). Resolving the gradients in the viscous BL is computationally expensive at high Re. Therefore, models of geophysical flows often adopt a slip BC ($S = 1$) or a drag law (akin to partial slip) for convenience, letting the BL be unresolved.

The dimensions of the domain are listed in Table 2 for five different cases. The **NOSL** case has no-slip bottom boundary ($S = 0$) everywhere, and the velocity profile in the inlet plane is the Blasius BL profile. In this case, the BL thickness δ is fixed at $0.03h$ at the inlet ($x = -L_x^-$) and grows to $0.1h$ at the obstacle. The **SL** and **SL-UN** cases have slip ($S = 1$) on all solid boundaries and, to be consistent, the inlet plane has uniform velocity U_0 rather than a BL profile. Note that **SL-UN** denotes the unstratified analog of the **SL** case. Fig. 2(a) shows the two inflow velocity profiles for the slip and no-slip cases. The **Hybrid** case uses a combination of BCs: the obstacle boundary is no-slip, while the flat bottom is a slip boundary. The bottom BL is prevented from forming and interacting with the wake, since $S = 1$ on the flat bottom. At the same time, the choice of $S = 0$ on the obstacle boundary allows boundary layer vorticity from the obstacle to feed into the wake.

Bottom friction effects require consideration in the numerical modeling of geophysical wakes. However, when the boundary layer is resolved as is the case here, the Reynolds number is necessarily moderate ($Re_D \sim 10^4$), and the effect of bottom friction is stronger than in geophysical flows. A drag law can be used to approximate the high-Re boundary layer, an approach which offers the following advantages: (1) a choice for local drag coefficient (C_d), which has a lower value than C_d of a laminar low-Re boundary layer and is more realistic for a turbulent boundary layer, and (2) it is an unsteady boundary condition unlike no-slip and, therefore, does not overly constrain the fluid near the boundary to be quasi-steady. We have performed an additional simulation using a quadratic drag law (case **DL**) with $C_d = 0.0025$ applied to the flat bottom and to the obstacle boundary. For details regarding the implementation, readers are referred to Rapaka and Sarkar (2016).

Convective outflow BCs are employed at the outlet (Orlanski, 1976). For scalar variables, the no-flux BC is imposed everywhere to keep the system adiabatic. Internal gravity waves are supported by the background stratification. In order to prevent spurious reflections of these disturbances, sponge regions are employed near the top and inlet boundaries where the relaxation terms $\sigma(x_i)(u_i(x_i, t) - U_i)$ and $\sigma(x_i)(\rho(x_i, t) - \rho_{bg}(z))$ are added to the governing equations to accomplish Rayleigh damping (Pal et al., 2017). Note that for **NOSL**, the upstream domain size L_x^- is smaller than for other cases. This limits the thickness of the boundary layer (BL) at the obstacle to $0.1h$.

2.3. Numerical details

The **NOSL** case, which has a shorter streamwise domain size, has a mesh with 564.7 million nodes and the **SL**, **SL-UN**, **DL** & **Hybrid** cases have 629.14 million nodes. In the **NOSL** case, the grid resolution is very fine at the boundary to resolve the large velocity gradients. At the flat bottom and the obstacle boundary, the grid spacing is $\Delta_x = 0.013h$, $\Delta_y = 0.019h$ and $\Delta_z = 0.0049h$. Since the BL thickness just upstream of the obstacle is $\delta = 0.1h$, it is evident that BL gradients (dominant in the vertical) in this quasi-laminar BL are well resolved.

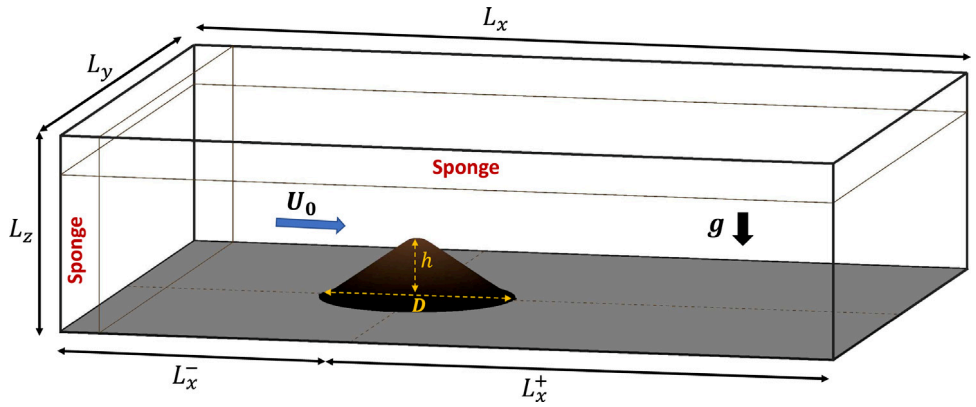

Fig. 1. Setup of the problem (not to scale): Uniform stratified flow encounters a conical obstacle. L_x, L_y and L_z are the streamwise, spanwise and vertical domain sizes. The uniform current U_0 is oriented in the streamwise (x) direction. The obstacle is placed at $x = 0$, with L_x^- being the upstream domain length and L_x^+ being the downstream distance traversed by the flow before reaching the outlet.

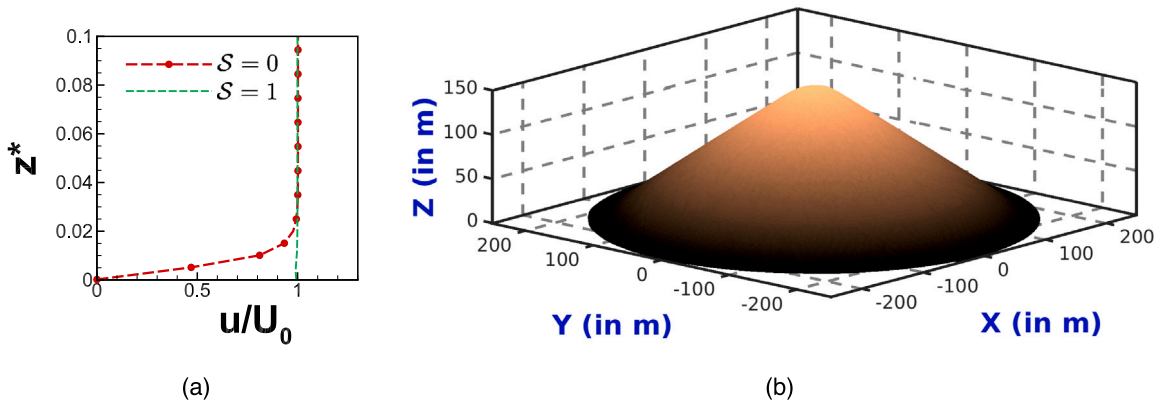

Fig. 2. Left: Incoming fluid velocity profile shown for cases with $S = 0$ and $S = 1$ at an upstream location $x^* = -2.4$. Right: Three-dimensional representation of the obstacle.

Table 2
Simulation parameters for different cases in this study. The streamwise domain size (split into values, upstream and downstream of the obstacle) is as given in the table, and the other domain sizes (L_y and L_z) are fixed at $6D$ and $20h$, respectively, for all cases. The grid sizes in the corresponding directions are N_x, N_y and N_z. The slip parameter S is either 0 or 1. The Reynolds number (Re_D) for all cases is 15,000.

Case	L_x^-	L_x^+	N_x	N_y	N_z	Fr_h	Description
NOSL	3D	14D	1280	1024	430	0.2	No-slip ($S = 0$) BC everywhere
SL	8D	14D	1536	1024	400	0.2	Slip ($S = 1$) BC everywhere
Hybrid	8D	14D	1536	1024	400	0.2	$S = 0$ on obstacle & $S = 1$ on bottom wall
SL-UN	8D	14D	1536	1024	400	Inf	Unstratified & Slip ($S = 1$) BC everywhere
DL	8D	14D	1536	1024	400	0.2	Quadratic drag law BC everywhere

The spatial derivatives are computed using second-order central finite differences on a staggered grid. For time advancement, a semi-implicit Runge–Kutta/Crank–Nicholson (RK3–CN) formulation is used. The spanwise domain extends up to $3D$ on each side and periodic BCs are imposed on these lateral boundaries, similar to the approach of Dairay et al. (2015). The elliptic pressure Poisson equation takes advantage of uniform grid spacing in the spanwise direction, thereby enabling Fourier decomposition. A 2D Poisson equation is formed for each Fourier mode and solved efficiently with a direct solver, namely the "divide and conquer" strategy proposed by Rossi and Toivanen (1999).

2.3.1. Topography

The bathymetry considered in all cases is a conical obstacle (Fig. 2(b)) with height (h) of 150 m and bottom diameter (D) of 500 m. The obstacle is generated by rotating a smooth triangle around its vertical axis. The slope of the obstacle is 30°, while the crest and foothill are smoothed out. The flow is resolved using a Cartesian staggered grid and the obstacle is modeled with an immersed boundary method. The numerical implementation of the BC on the body is summarized as follows: The grid points inside the body are tagged as 'solid points', those outside the boundary are 'fluid points'. The 'fluid points' in the vicinity of the boundary are called 'forcing points'. These are the points where the BCs are applied during the predictor step of RK3-CN.

Fig. 3 shows a schematic of the tagged points in the vicinity of the obstacle boundary. For every forcing point **F**, point **B** is obtained by tracing a normal to the surface passing through **F**. Subsequently, the interpolation point **P** is obtained by backtracking $\overline{BF}$ to the cell with the nearest face intersection. The velocity components at **P** (denoted as $\boldsymbol{u}^{\boldsymbol{P}}$) are determined from its fluid neighbors by linear interpolation and the velocity components at **B** are assigned using Eq. (6). Finally, the velocity components at the forcing point **F** are determined by weighted

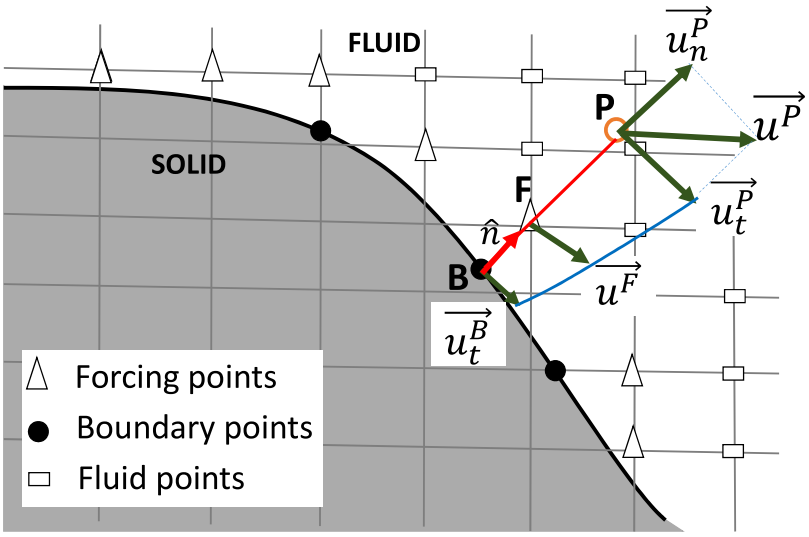

Fig. 3. Generalized interpolation stencil used in IBM for implementing the appropriate BC on the forcing points. Here, **B** is the boundary point, **F** represents the forcing point and **P** is the interpolation point. **BF** line segment is normal to the fluid–solid interface (dark black line).

averages of $\boldsymbol{u^B}$ and $\boldsymbol{u^P}$. For additional details, the reader is referred to Yang and Balaras (2006).

2.3.2. LES Model

Large eddy simulations (LES) are conducted with effects of the unresolved fine scales represented with a subgrid scale (SGS) model. Thus, the viscous stress and density flux vector in Eqs. (1) and (3) are computed as:

$$\tau_{ij} = (\nu + \nu_{sgs})\frac{\partial u_i}{\partial x_j} \quad , \quad \chi_j = (\kappa + \kappa_{sgs})\frac{\partial \rho}{\partial x_j}. \tag{7}$$

Here, ν_{sgs} is estimated using the dynamic eddy viscosity model of Germano et al. (1991) as $\nu_{sgs} = C_s\overline{\Delta}^2|\overline{S}|$, where $|S| = \sqrt{2S_{ij}S_{ij}}$. The coefficient C_s is dynamically computed (Lilly, 1992). The customary smoothing of C_s is performed in this problem with Lagrangian averaging (Meneveau et al., 1996) along particle trajectories using an exponential weighting function. Lagrangian averaging is effective in flows which do not have a homogeneous spatial direction to implement smoothing. In all simulations, the subgrid Prandtl number ($Pr_{sgs} = \nu_{sgs}/\kappa_{sgs}$) is fixed as unity.

The mean value (Reynolds average) of any field variable is obtained by averaging in time after the initial transient has subsided. The mean value of the parameter ϕ is denoted by $\langle\phi\rangle$, and the fluctuating field becomes $\phi' = \phi - \langle\phi\rangle$. The turbulent kinetic energy is denoted by $K = \langle u_i' u_i'\rangle/2$.

3. Flow velocity

Fluid that is able to go over the obstacle generates internal waves that propagate in the stratified background. For $Fr < 1$, stratification introduces a critical height $z_s = h(1 - \alpha_T Fr_h)$ that determines whether fluid can travel vertically over an obstacle or is limited to horizontal motion around the topography. Here, α_T is a factor of order 1 and is dependent on the shape of the obstacle (Hunt and Snyder, 1980). Above z_s, fluid kinetic energy is sufficient to overcome the potential energy barrier. Vertical motion in this region of the flow is effective at generating internal waves that can propagate in the stratified background. Below z_s, the fluid is confined vertically or 'blocked' and is deflected sideways to eventually separate with primarily horizontal motion. The instantaneous streamlines discussed in Section 3.1 reveal that flow separation as well as the post-separation flow changes qualitatively when the BC is changed from **NOSL**. The influence of BC type is quantified in Section 3.2 where the mean velocity fields are discussed. The temporal variability in the wake also depends substantially on the BC as elaborated in Section 3.3. Turbulence levels are quantified through the turbulent kinetic energy (TKE) in Section 3.4.

3.1. Streamlines

Fig. 4 shows instantaneous streamlines in **NOSL** and **SL**. These streamlines originate upstream of the body and are colored with the vertical velocity (w) value. One set of streamlines originates from a vertical line ($y^* = -0.01$ and $x^* = -0.6$) located centrally and upstream. Some of the upper streamlines in this set (those that originate above z_s) have sufficient positive (red) w to surmount the obstacle after which they slope downward to follow a downslope jet. The subsequent oscillation of these streamlines is indicative of a lee wave. Streamlines that originate below z_s on the vertical line are unable to surmount the obstacle and their lateral (sideways) deflection can be seen as they negotiate the obstacle. Another set of streamlines in Fig. 4 originates from a spanwise-oriented upstream line located at $z^* = 0.066$ (a height below z_s) and $x^* = -0.6$. These streamlines illustrate the downward and lateral motion of fluid that originates from the blocked region. The isosurface of $u = 0$ is plotted in silver blue and serves to demarcate the recirculation zone.

Flow separation in **NOSL** has a pattern that is distinct from **SL**, although both cases exhibit upstream blocking. Fluid in **NOSL** experiences viscous drag and, owing to the larger reduction of flow speed, separates earlier relative to **SL**. The streamlines in **SL** show that the fluid is able to navigate around the obstacle curvature for a longer distance and curve inward before eventual separation. Consequently, the separation line, which is the intersection of the $u = 0$ isosurface in silver blue with the obstacle, has a smaller lateral size in **SL**.

The post-separation flow is strikingly different between **NOSL** and **SL**. The recirculation region is significantly shorter in **SL**. The small-scale corrugations in the $u = 0$ isosurface and the rapid changes in the direction of w along streamlines indicate that the near wake in **SL** has stronger turbulence than **NOSL**. Fig. 4(b) shows that some of the streamlines adjacent to the bottom exhibit large lateral excursion around the recirculation region. These excursions illustrate unsteady, large-amplitude lateral meanders of fluid in the wake that are prominent in **SL** and absent in **NOSL**.

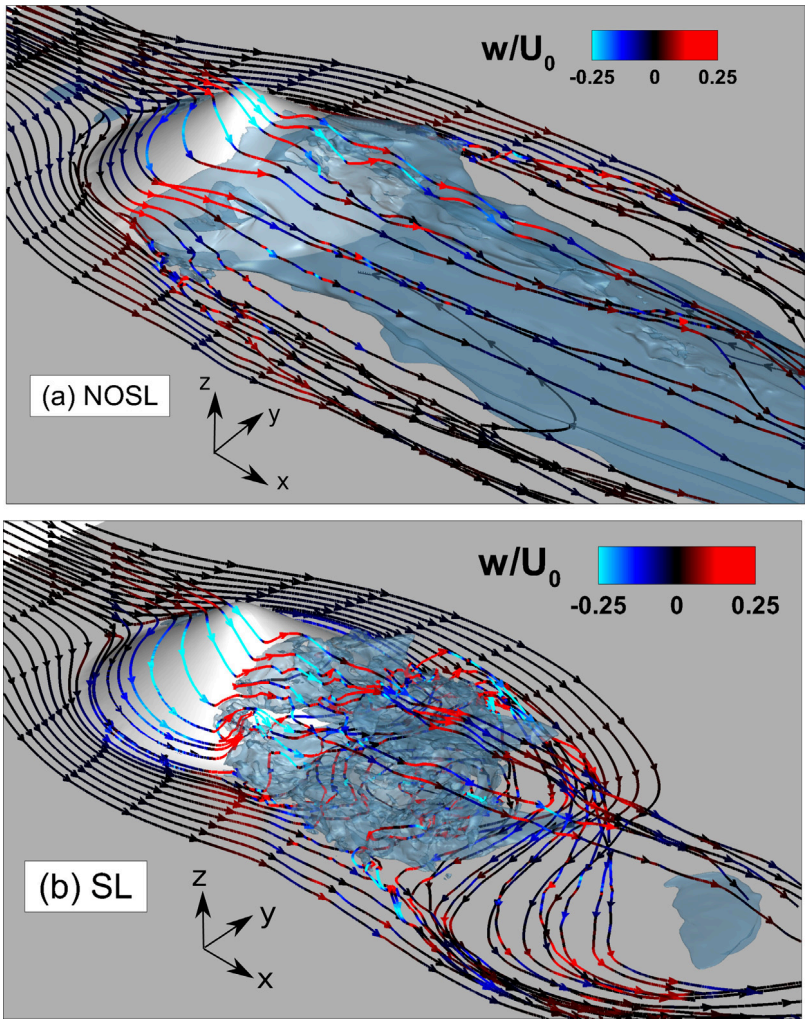

Fig. 4. Instantaneous streamlines which originate from upstream are plotted at $t^* = 100$: (a) **NOSL** and (b) **SL**. The streamlines are colored with the vertical velocity. The silver blue color represents the isosurface $u = 0$, which demarcates the recirculation zone behind the obstacle up to $x^* = 2.2$ downstream.

3.2. Mean velocity

To investigate the influence of the BC on the flow statistics, we examine the mean streamwise and vertical velocity fields, shown in Fig. 5. Initially, the flow in the downstream wake is allowed to become statistically steady. The equilibrium time needed to attain this state is estimated to be $70D/U_0$. After $t^* = 70D/U_0$, statistics are recorded and the temporal average is performed over a time span of $40D/U_0$. Comparison among Fig. 5(a–d) shows that the recirculation bubble in the lee of the obstacle is largest in **NOSL**, followed by **DL** & **Hybrid** and then **SL**. The unblocked layer of fluid, which is able to traverse the obstacle vertically, generates steady lee waves with phase lines that are prominent in the vertical velocity contours of Fig. 5(e–h). The lee waves far away from the obstacle (beyond $x^* = 2.5$) are similar in the centerplane ($y^* = 0$) among the three cases. However the lee-wave near field is different in **NOSL** (Fig. 5 e) relative to the other cases. Here, the larger recirculation zone does not allow the lee waves to penetrate into a substantial portion of the near wake. However, in **SL**, **DL** and **Hybrid**, the lee-wave phase lines in Fig. 5 (f–h) that are downstream of $x^* = 2$ (end of the recirculation region), extend close to the flat bottom.

Although the **Hybrid** and **DL** cases exhibit a slightly larger recirculation zone downstream, the wake in these cases is qualitatively similar to **SL**. Therefore, the comparison in subsequent sections will be primarily between cases **SL** and **NOSL**.

The lateral structure of the flow is illustrated by Fig. 6 which shows the variation of mean streamwise and vertical velocity on the horizontal plane located at the height $z^* = 0.5$. Fig. 6(a)–(b) shows that, independent of the BC, the wake grows laterally after the recirculation zone ends. Owing to the shorter streamwise length of the recirculation zone, the lateral growth commences earlier in **SL**. The lateral structure of the lee waves is illustrated by the vertical velocity field shown in Fig. 6(c)–(d). Away from the body, the lee wave signature is less clear in **SL**. For example, phase lines in the region $|y^*| > 1$ are less distinct in Fig. 6(d) relative to Fig. 6(c). The slip BC in **SL** allows significant unsteady lateral (v) velocity outside the mean wake which interferes with the establishment of the wave field in this region of $|y^*| > 1$. Immediately behind the body, it is in **NOSL** where the wave field is disrupted. Thus, in **NOSL** (Fig. 6c), the signature of the wave in the central region behind the obstacle is absent in the recirculation bubble but eventually appears beyond $x^* = 2$. **NOSL** (Fig. 6c) also shows upstream spanwise-invariant stripes in the vertical velocity, which are associated with an internal-wave response of the developing boundary layer as it approaches the obstacle. These stripes are negligible in the other cases.

The behavior of mean defect velocity U_d, where $U_d = U_0 - \langle u(x, y, z, t)\rangle$, depends on the BC, as is qualitatively apparent from Fig. 6(a)–(b). To further quantify the influence of the BC, the evolution

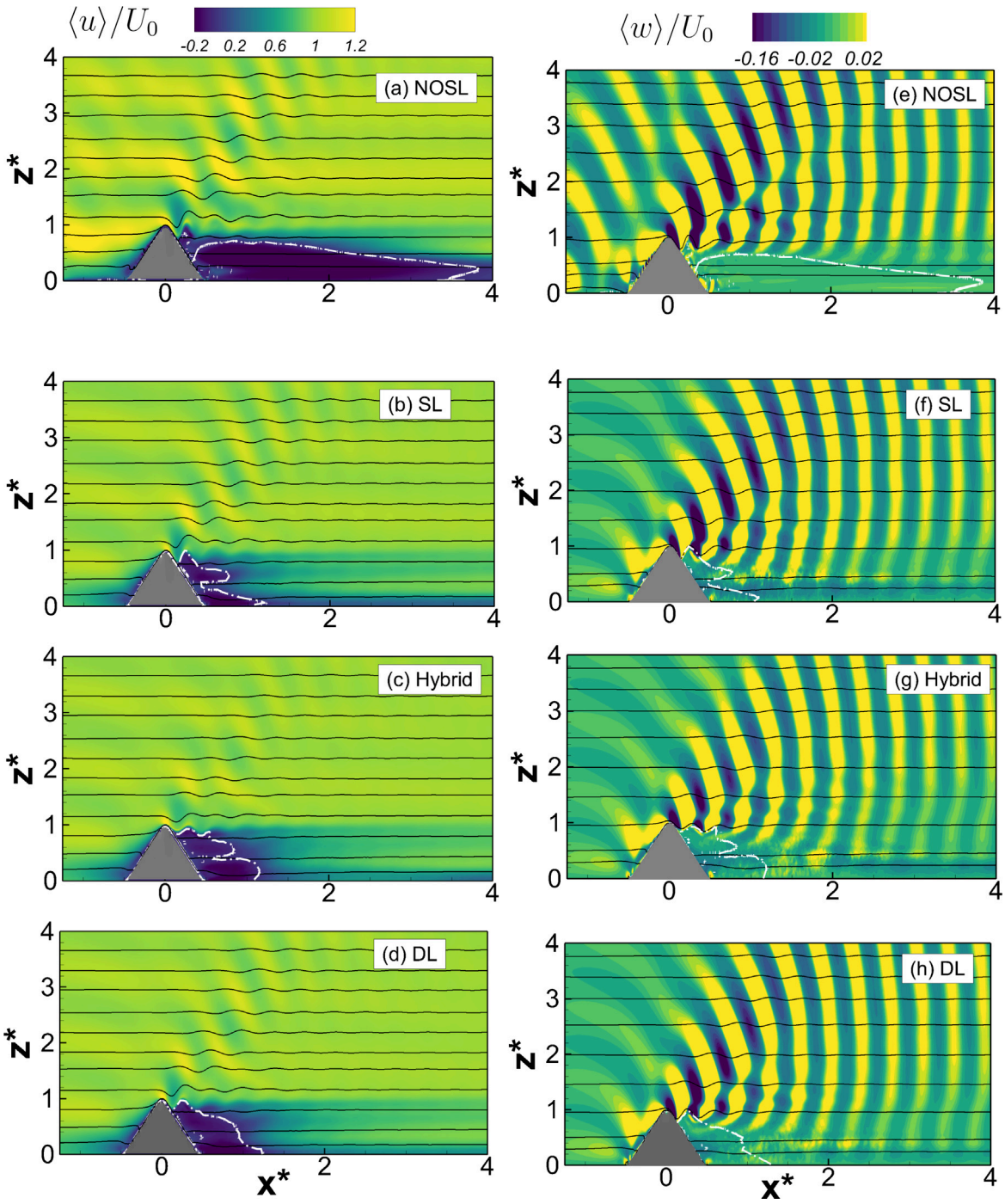

Fig. 5. Mean streamwise velocity (a–d) and vertical velocity (e–h) in the centreplane ($y^* = 0$): The four cases — **NOSL** (first row), **SL** (second-row), **Hybrid** (third row) and **DL** (fourth row) show substantial differences in the size of the recirculation region of the wake (a–d) and the penetration of the internal waves into the wake (e–h) at the same Re_D and Fr_h. Note that the aspect ratio is changed for better visualization. The dotted white line denotes the $u = 0$ contour.

of normalized U_d is plotted along the horizontal line located at $z^* = 0.25$ and $y^* = 0$ in Fig. 7. The recirculation zone can be demarcated using the condition $U_d/U_0 > 1$. The recirculation zone for **NOSL** is more than three times longer than in **SL**, **DL** and **Hybrid**. In **NOSL**, the value of U_d decreases in a monotone fashion after the recirculation zone. Similarly, there is a decrease of U_d after the recirculation zone in **SL**, **DL** and **Hybrid**. However, U_d decreases more rapidly relative to **NOSL** indicating that **SL** has fluid with higher velocity (relative to **NOSL**) in the lee. The reason is that higher-velocity freestream fluid is brought periodically into the lee by the lateral flapping of the wake and increases the time-averaged velocity. It is worth noting that the signature of the lateral flapping on streamlines, namely a large-scale lateral meander, was shown in Fig. 4. The rapid decrease of U_d in **SL** lasts until $x^* \approx 5$. The amplitude of the lateral motion decreases with increasing x^* and, after $x^* \approx 5$, the strength of the initial decrease of U_d can no longer be maintained and the value of U_d tends to increase somewhat. The imprint of the steady lee waves on the defect velocity is seen as a modulation of U_d with the wavelength of $2\pi Fr_D$ (Fig. 7b).

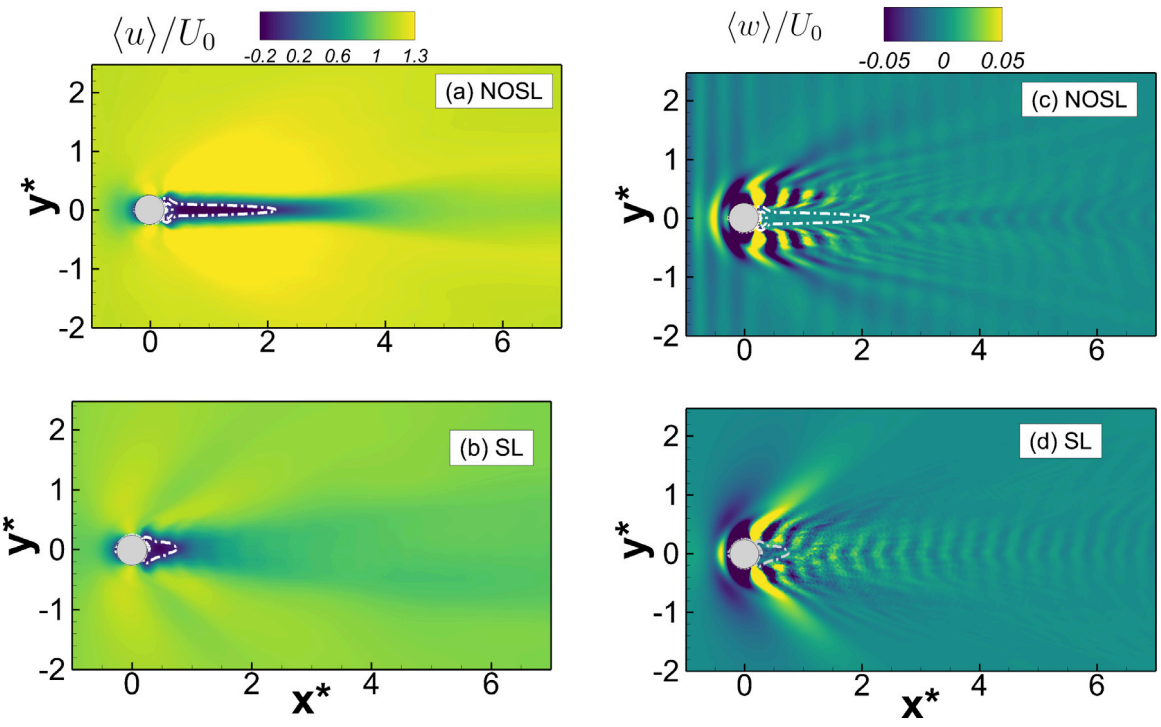

Fig. 6. Mean streamwise velocity (a–b) and vertical velocity (c–d) in the horizontal plane $z^* = 0.5$. Aspect ratio of figure axes is 1:1. The dotted white line denotes the $u = 0$ contour.

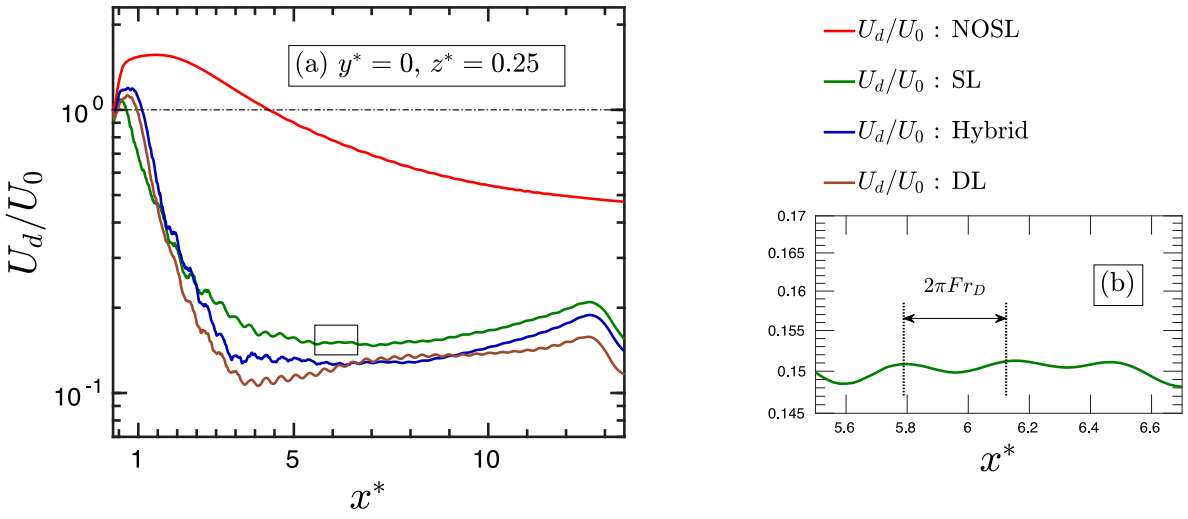

Fig. 7. Streamwise evolution of horizontal velocity in the centerplane ($y^* = 0$) and at height $z^* = 0.25$ shown for all 4 choices of BC: (a) Mean centerline defect velocity (U_d), and (b) A small window shown in part (a) is magnified to depict oscillatory modulation of the wake by the lee wave. Here, Fr_D is defined as U_0/ND.

3.3. Velocity spectra

In Fig. 8, the spectra of streamwise (u) and spanwise (v) velocity are plotted at a downstream location ($x^* = 1$, $y^* = 0.39$ and $z^* = 0.166$) close to the obstacle. The Strouhal number St is defined as $f_s D/U_0$, where f_s denotes the frequency computed from the Fourier transform of the temporal flow history at the probe. The probe location has been chosen such that it lies on the trajectory of the shed vortices. Case **SL** shows a broadband spectrum with a wide separation of time scales in the flow, indicative of a fully turbulent flow. In contrast, the amplitude of the spectrum in **NOSL** is smaller by a factor of 10^3 and, furthermore, spans a narrower range of frequencies. The amplitudes of S_{uu} and S_{vv} are comparable in **SL**. Both S_{uu} and S_{vv} in **SL** reveal a discrete peak at $St = 0.24$ which corresponds to the shedding frequency of the lee vortices off the obstacle. The observed $St = 0.24$ is close to the estimate of $St = 0.264$ computed from the $St - Re_D$ relationship proposed by Williamson and Brown (1998) for cylinder wakes. There is no such periodic component in **NOSL** at this location.

Moving to a further downstream location, we find a periodic signal in both components of horizontal velocity and a corresponding spectral peak in both **SL** and **NOSL**. This temporal periodicity is illustrated by Fig. 9(a) for the v component at a downstream location: $x^* = 9, y^* = 0$ and $z^* = 0.5$. In **NOSL**, the spectral peak of v at this location is at $St = 0.5$, and corresponds to the barotropic sinuous instability of the quasi-two-dimensional wake (Lesieur, 2008). The barotropic instability of wakes and jets takes the form of a sinuous mode that evolves into two staggered rows of vortices of opposite sign (Maslowe, 1991; Perret et al., 2011; Carpenter and Smyth, 2019) and, under forcing, also a

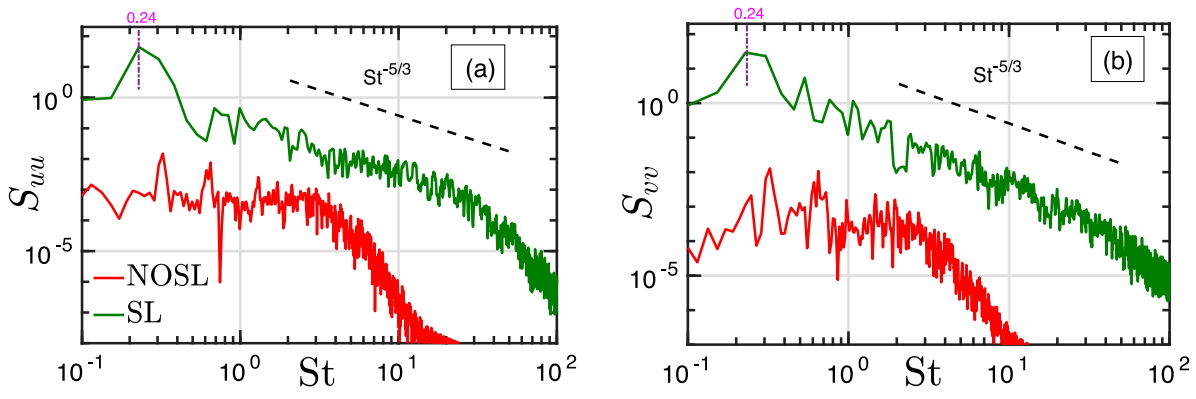

Fig. 8. Spectra at a location ($x^* = 1$, $y^* = 0.39$, $z^* = 0.166$) close to the obstacle compared between **NOSL** and **SL** cases: (a) streamwise velocity (S_{uu}), and (b) spanwise velocity S_{vv}.

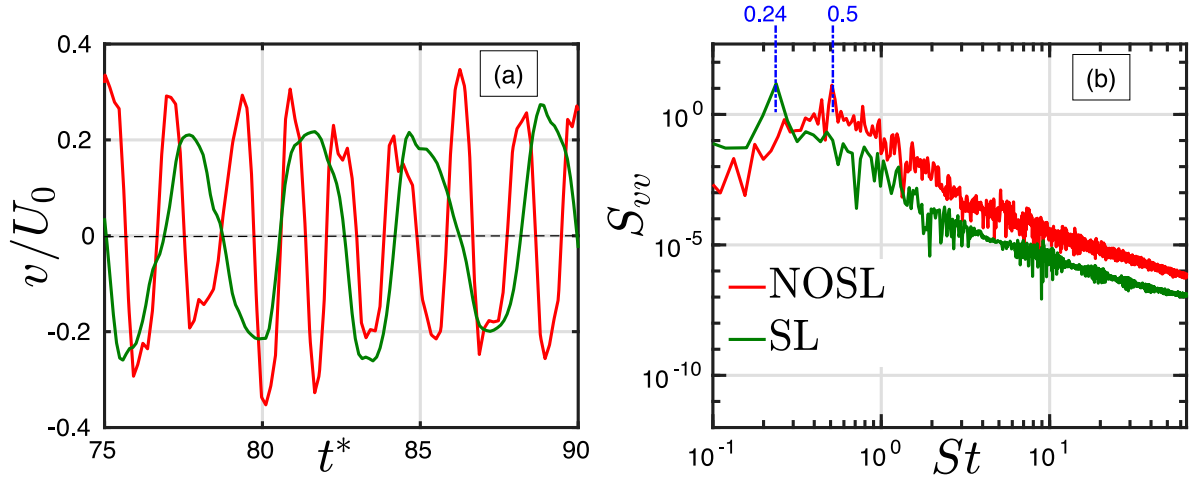

Fig. 9. Spanwise velocity at a far downstream location ($y^* = 0$, $x^* = 9$, $z^* = 0.5$) is contrasted between **NOSL** and **SL** cases: (a) time history, and (b) corresponding velocity spectra. At this downstream location, the turbulent fluctuations in the flow have diminished leaving behind a clear signature of the instabilities of the velocity profile of a quasi-two dimensional wake.

varicose mode with two non-staggered vortex rows. The frequency of this instability in **NOSL** is found to vary with height so that St takes values between 0.4 and 0.8. However for case **SL**, the vortex shedding frequency does not change with height.

3.4. Turbulent kinetic energy

To quantify the influence of BCs on the wake turbulence, snapshots of TKE are shown in the central vertical plane ($y^* = 0$) in Fig. 10. Additionally, mean velocity vectors are shown at selected streamwise locations to illustrate the overall flow structure. In **NOSL**, there is strong bottom shear in the recirculation region. However, the bottom boundary layer is quasi-laminar at this moderate Re and, furthermore, bottom friction restricts the lateral meander of the wake that would generate turbulent fluctuations. Therefore, in the near-bottom region of $0 < z^* < 0.2$, **NOSL** exhibits small TKE. In the upper region, a shear layer forms at the boundary of the recirculation zone with the downslope jet and lee wave to support turbulent fluctuations, shown by a zone of enhanced TKE (Fig. 10a), which spreads vertically with increasing x^*. These fluctuations also trigger instability of the horizontal shear in the wake to eventually allow the spanwise oscillation (Fig. 9) which is seen further downstream. In **SL**, the recirculation zone is small. The slip BC allows near-bottom lateral meanders close to the body as well as broadband fluctuations which are reflected in the high TKE content of the flow in the lee of the obstacle. Unlike **NOSL**, a strong upper shear layer does not develop and the TKE is bottom-intensified.

4. Vortex dynamics

Lee vortices, which are coherent patches of vertical vorticity (ω_z) with size comparable to the lateral dimensions of the obstacle, represent a noticeable pattern in geophysical wakes. Lee vortices are present in the simulations of stratified flow past an obstacle. However, boundary conditions affect the spatial organization and the temporal signature of the lee vortices as elaborated in Section 4.1. Apart from the organized ω_z in lee wake vortices, there are swirling motions with horizontal vorticity which are associated with internal waves, separated shear layers with vertical shear, boundary layers, and also disorganized turbulence. The effect of BCs on ω_y is discussed in Section 4.2.

The mechanism underlying the formation of lee vortices is of interest. Boundary-layer vorticity is generally thought to be the primary source of wake vorticity. However, in the stratified mountain wake simulated by Smolarkiewicz and Rotunno (1988), a slip BC was used and attached lee vortices were found. The authors attributed the formation of coherent vortices to the generation of horizontal vorticity by baroclinic torque followed by tilting of horizontal vorticity to the vertical. Obstacle curvature can also induce vorticity into the flow, and Smith and Smith (1995) allude to this mechanism as a possible source of lee vortices. Vorticity induced by this mechanism is proportional to the tangential velocity of the flow at the obstacle surface as elaborated later in Section 4.3. We conduct an additional unstratified simulation (**SL-UN**) to ascertain if curvature alone (without baroclinicity) can lead to lee vortices, and present its results in Section 4.3. **SL-UN** has the

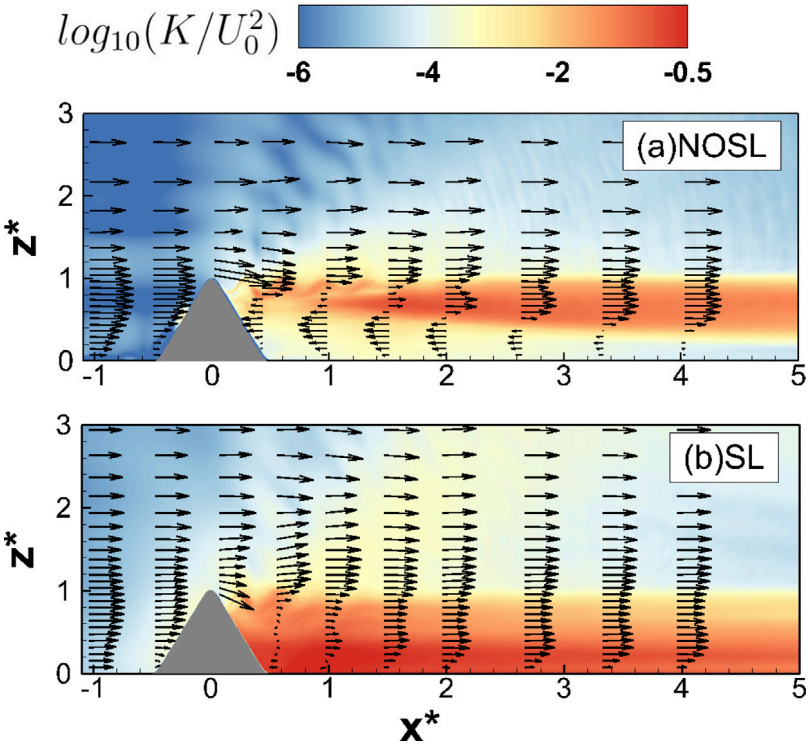

Fig. 10. Spatial organization of turbulent kinetic energy ($K = \langle u_i' u_i' \rangle / 2$) normalized by U_0^2 in the vertical plane $y^* = 0$: (a) **NOSL**, and (b) **SL**. Vectors representing the mean velocity field are also shown at selected cross-sections.

same obstacle geometry and current speed as **SL**, but the background is unstratified. Section 4.4 includes a quantitative analysis of the vorticity sources to further clarify the generation mechanism of lee wake vortices. The area ($y - z$) integrated value of the squared vorticity in each component is computed and the streamwise evolution is contrasted among various cases. Furthermore, the relative magnitudes of the principal source/sinks of vorticity are evaluated to directly assess the importance of baroclinic torque relative to the other sources.

4.1. Lee wake vortices

The organization of vertical vorticity (ω_z) in **NOSL** is strikingly different from **SL, DL** and **Hybrid** cases, while the latter three cases resemble each other. Fig. 11 illustrates the difference by showing ω_z contours on horizontal planes at four different heights in the wake.

In **NOSL** (Fig. 11a), there is a pair of counter-rotating vortices at $z^* = 0.066$ close to the bottom. These lee vortices are found to be steady in time and take the form of an attached recirculation bubble. The presentation of these vortices resembles the lee vortex pair found near the bottom in the laboratory experiment of Hunt and Snyder (1980) and also in aerial observations by Smith and Grubisic (1993) of the wake of Hawaii. At the somewhat higher location of $z^* = 0.33$ too, there is a steady recirculation bubble. However, at the even higher location of $z^* = 0.66$, the recirculation bubble, while remaining attached, displays unsteadiness at its tail end, and coherent vortices appear further downstream. The size of the lee vortices at a given height is proportional to the local diameter ($d(z)$) of the conical obstacle. This large-scale unsteadiness, observed further downstream, sets in at heights above $z^* = 0.2$ through barotropic sinuous instability (Lesieur, 2008; Carpenter and Smyth, 2019) of the velocity profile of a quasi-two-dimensional wake that develops into coherent vortices.

In contrast, the bottom slip wall in **SL** allows unsteady shedding of alternating opposite-signed Kármán vortices from the obstacle. Their instantaneous presentation is qualitatively different from **NOSL**, as can be seen by comparing the $z^* = 0.066$ and 0.33 planes (Fig. 11b) to the corresponding planes in **NOSL** (Fig. 11a). The shedding of Kármán vortices from the body leads to lateral flapping of the wake which is manifested by the lateral meanders in the streamlines and the oscillation of the centerline lateral velocity which were described previously. At $z^* = 0.93$, the lee waves interfere strongly with the coherent structures in the wake, thereby disturbing the vortex street.

To summarize, lee vortices form behind the obstacle, independent of the BC. Furthermore, their lateral size at a given height is proportional to the local diameter of the obstacle. The critical difference introduced by the type of BC is that the lee vortices in **SL** are shed off the body unsteadily to result in a Kármán vortex street while, in **NOSL** there is a quasi-steady, attached vortex pair.

The results of previous sections on the mean velocity show that the behavior of **DL** resembles **SL** and **Hybrid**. Fig. 12(c) depicts contours of ω_z in the horizontal plane $z^* = 0.25$ in the drag-law case. The corresponding ω_z contours for the other BCs, which are included for comparison in Fig. 12, demonstrate that **DL**, **Hybrid** and **SL** cases are qualitatively similar in terms of vortex dynamics.

4.2. Spanwise vorticity

In addition to the vertically oriented lee vortices, there is substantial horizontal vorticity. The organization of horizontal vorticity depends on BCs as illustrated by the two orthogonal planar views of ω_y in Fig. 13. For example, the boundary layer on the flat bottom provides a significant swath of ω_y (seen in the horizontal plane with positive values under the current and small negative values under the weak recirculating flow) in **NOSL**, a feature that is absent in **SL** (Fig. 13). Above the obstacle, both cases exhibit ω_y associated with the lee wave. There is also a thin strip of ω_y on the obstacle which is created by the upslope flow followed by the downstream jet. This strip separates from the obstacle slightly below its apex and subsequently exhibits the wavelength of the impressed lee wave.

The flow behind the obstacle in **SL** shows a disorganized pattern with small-scale patches of intense ω_y (Fig. 13(b)). The small-scale variability is much less pronounced in **NOSL**. Evidently, for the conditions

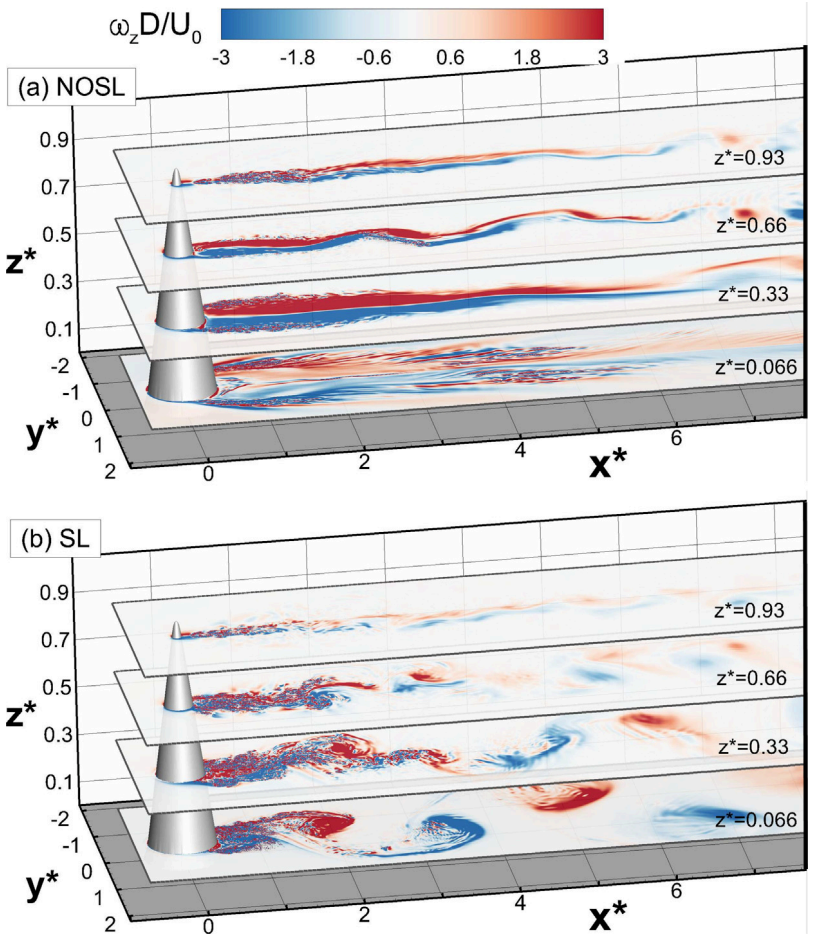

Fig. 11. The organization of the lee vortices is affected by the boundary conditions. Lee vortices are shown by contours of normalized vertical vorticity (ω_z) at $t^* = 100$: (a) **NOSL**, and (b) **SL**.

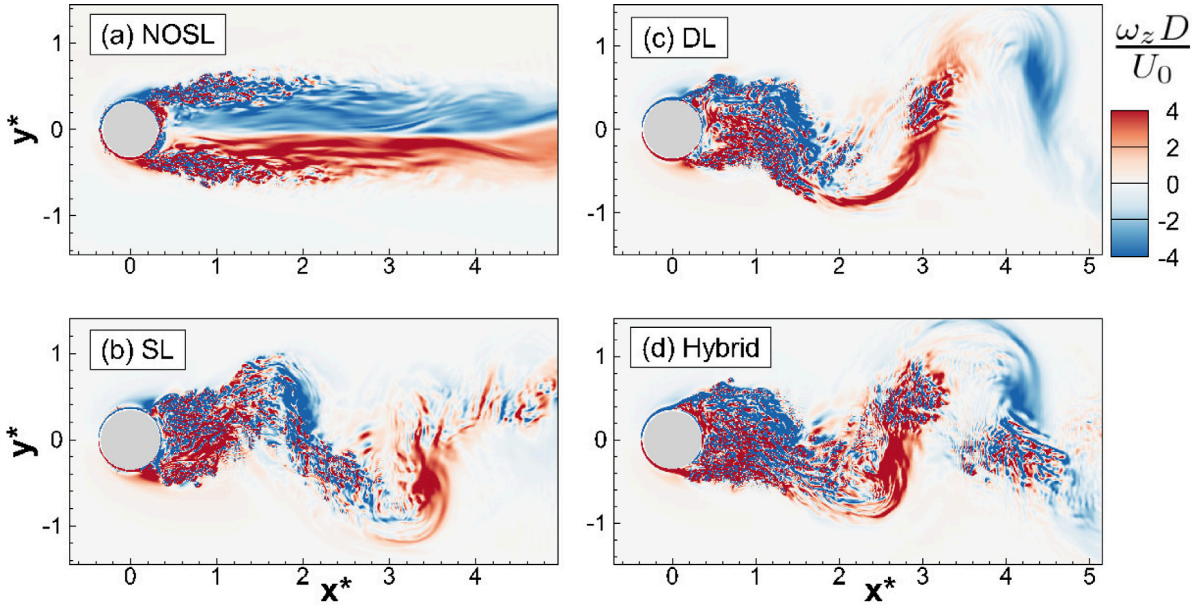

Fig. 12. Spatial organization of vertical vorticity ω_z in the horizontal plane $z^* = 0.25$ at time $t^* = 75.8$: (a) **NOSL**, (b) **SL**, (c) **DL**, and (d) **Hybrid**.

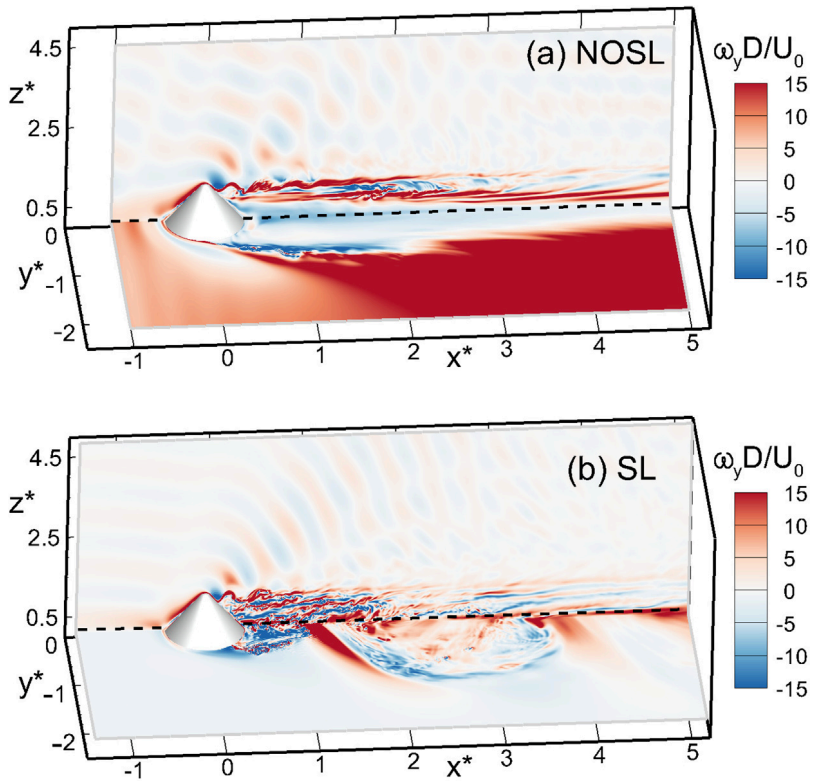

Fig. 13. Comparison of spanwise vorticity (ω_y) between cases with different BCs: (a) **NOSL** and (b) **SL**. Instantaneous contours of ω_y are depicted on a vertical plane ($y^* = 0$) and a horizontal plane ($z^* = 0.13$). The black dotted line represents the intersection between the vertical and the horizontal plane.

of this study, the boundary layer on the flat bottom is able to restrict wake turbulence.

4.3. Unstratified wake

We have seen that, for all BCs considered here, there are coherent wake vortices in low-Fr_h flow past a conical obstacle, and they take the form of unsteady Kármán vortices, shed from the body, in the **SL** case. Both body curvature and baroclinicity have been advanced in the past as potential origins of the wake vorticity. To exclude the effect of baroclinicity, an unstratified counterpart (**SL** − **UN**) has been simulated with the slip BC.

Vorticity can be induced by solely body curvature, and is proportional to the tangential slip velocity of the flow at the obstacle (Leal, 1989; Legendre et al., 2009). To demonstrate curvature-induced vorticity, consider free-slip flow past a circular shear-free cylinder of radius a in polar coordinates (r, θ). Since $u_r = 0$ and $\tau_{r\theta} = 0$ at $r = a$, it follows that $\partial u_\theta/\partial r = u_\theta/a$ and $\omega_z = (\partial u_\theta/\partial r + u_\theta/r)_{r=a} = 2u_\theta/a$. Here, u_θ represents the surface tangential velocity. As elaborated below, the unstratified counterpart is qualitatively different from the stratified cases. In particular, although curvature alone does give rise to vorticity, lee vortices with size comparable to the body do not form in the wake.

Fig. 14(a) shows that, for case **SL** − **UN**, flow separation in the vertical centerplane ($y^* = 0$) occurs at $x^* = 0.35$ and $z^* = 0.3$. This is in contrast to the near-apex separation in the corresponding stratified case **SL** (left column of Fig. 5). Fig. 14(b) shows that separation is also delayed in the horizontal ($z^* = 0.066$) plane where it occurs close to the rear stagnation point. The flow remains attached to the sloping and curved geometry in **SL** − **UN** for a long distance before separation because of the following reasons: (a) absence of viscous loss of momentum at the boundary, and (b) lack of a lee wave and its imposition of an adverse pressure gradient on the boundary flow. It is worth noting that, in previous work on unstratified flow past a 3D obstacle with a no-slip BC, e.g. Garcia-Villalba et al. (2009), flow separation at the obstacle occurs substantially upstream relative to **SL** − **UN** and there is a large recirculation zone followed by a turbulent wake.

The recirculating flow at the junction of the bottom and central lee of the obstacle generates a narrow wake that develops a sinuous instability in the horizontal plane. Fig. 14(b) and (c) show the streamwise and spanwise velocity, respectively, in a horizontal plane $z^* = 0.066$. Here, this narrow region of attached low-velocity fluid in the lee can be noticed along with the subsequent sinuous instability.

The three components of vorticity are shown in Fig. 14(d–f) on a horizontal plane. The location of the plane at $z^* = 0.066$ is sufficiently below the apex so as to include the separated flow in the lee of the obstacle. There is vertical vorticity at the body in Fig. 14(d) owing to its curvature in the horizontal plane. However, the wake behind the body is narrow and does not exhibit the large lee vortices seen in the stratified cases. This observation confirms that curvature alone, without baroclinicity, is insufficient for the emergence of large lee wake vortices that have been observed in geophysical flows. Spanwise vorticity (ω_y) is predominantly positive adjacent to the obstacle, owing to the curvature of the hill in the vertical plane. The narrow wake has both spanwise (Fig. 14 e) and streamwise (Fig. 14 f) vorticity.

4.4. Sources of vorticity

The vorticity transport equation, obtained by employing the curl operator on Eq. (2), is as follows:

$$\frac{\partial \omega_i}{\partial t} + u_j \frac{\partial \omega_i}{\partial x_j} = \omega_j \frac{\partial u_i}{\partial x_j} + \mathcal{E}_{ij3} \frac{\partial b}{\partial x_j} + \nu \frac{\partial^2 \omega_i}{\partial {x_j}^2} + \mathcal{E}_{ikm} \frac{\partial}{\partial x_k} \left[\frac{\partial}{\partial x_j} \left(\nu_{sgs} \frac{\partial u_m}{\partial x_j} \right) \right] . \quad (8)$$

On the right hand side (r.h.s.) of Eq. (8), the first term represents vortex stretching/tilting and the second term is the baroclinic torque. The third and fourth terms are molecular diffusion and the modeled subgrid diffusion, respectively; both are lumped together into a single diffusion term in the results.

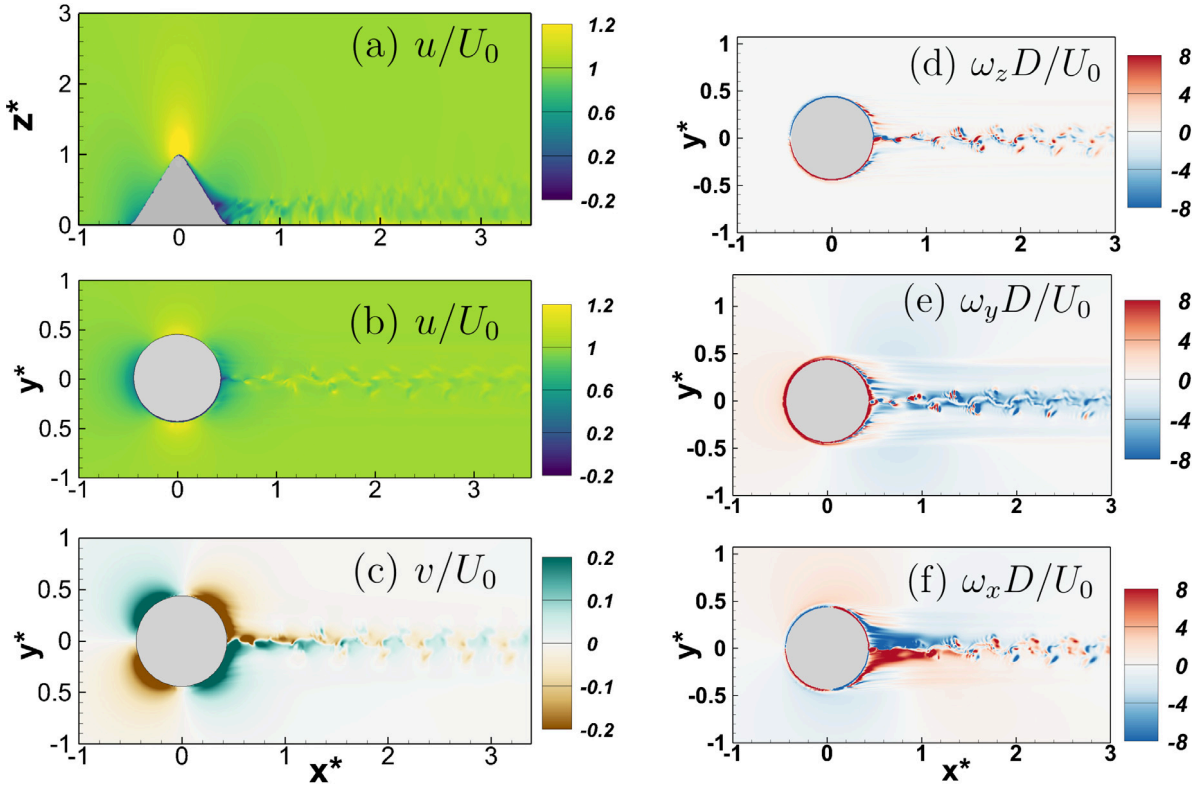

Fig. 14. Flow in case **SL-UN** is shown at $t^* = 101$. Left column shows normalized velocity components on different planes: (a) streamwise velocity on the vertical centerplane, ($y^* = 0$), (b) streamwise velocity on a horizontal plane ($z^* = 0.066$), and (c) lateral velocity on the same horizontal plane shown in (b). Right column shows normalized vorticity components on this horizontal plane, $z^* = 0.066$: (d) vertical vorticity, (e) spanwise vorticity and (f) streamwise vorticity.

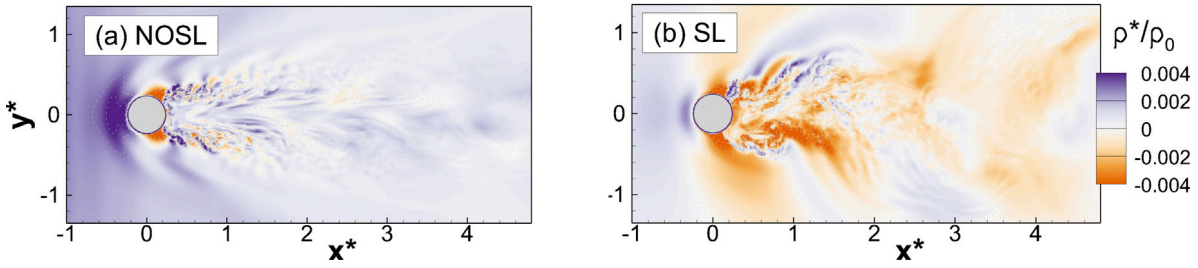

Fig. 15. Streamwise and lateral gradients in density, visible from contours of the density deviation (ρ^*) from the background, in the horizontal plane $z^* = 0.5$: (a) **NOSL**, and (b)**SL**.

In the case of an unstratified background, boundary-layer vorticity diffuses from the obstacle into the flow, and is subsequently reoriented and intensified by the vortex stretching/tilting term. A stratified background provides an additional vorticity source, namely the baroclinic torque associated with horizontal density gradients. Fig. 15 is an illustration of the horizontal density contrast on $z^* = 0.5$, located below the dividing streamline. The complex three-dimensional flow in the vicinity of the obstacle is responsible for the observed density contrast. Consider **NOSL** (Fig. 15 a). There is colder, denser fluid (purple) immediately upstream of the body on the horizontal plane, $z^* = 0.5$. Visualization of the streamlines in the vicinity of $z^* = 0.5$ shows an upward rise in front of the hill which brings heavier fluid (purple) from below. As the fluid negotiates the hill, the streamlines dip downward bringing lighter fluid (orange) at the sides of hill to the plane $z^* = 0.5$. In **NOSL**, there is an extensive recirculation zone behind the hill which tends to inhibit the lighter fluid from reaching $z^* = 0.5$ in the lee. Therefore, the patch of light fluid (orange) does not extend from the sides to behind the hill. Moving to **SL**, we find that the upstream density contrast is weaker. The reason is the absence of a developing upstream boundary layer which in **NOSL** displaces the streamlines and amplifies the upward transport of colder fluid. In **SL** too, streamlines dip down as the fluid proceeds past the curved sides of the hill. The larger amplitude of vertical and lateral motions behind the obstacle in **SL** leads to patches of light fluid in the lee (Fig. 15 b), which are larger than in **NOSL**. Consequently, the spanwise gradient (b_y) is larger in **SL** and so is its contribution to baroclinic torque. This is the reason why, as shown later in the top row of Fig. 16, ω_x behind the obstacle is larger in **SL** relative to **NOSL**.

Fig. 16 shows the streamwise evolution of $y - z$ plane-integrated values of enstrophy components (ω_x^2, ω_y^2 and ω_z^2) in Fig. 16(1a–c), vortex stretching in Fig. 16(2a–c), vortex tilting in Fig. 16(3a–c), diffusion term (includes viscous diffusion and the contribution from eddy diffusivity) in Fig. 16(4a–c), and baroclinic torque in Fig. 16(5a–b). In row 3 of Fig. 16, the vortex tilting term (t_x, t_y, t_z) is shown for each vorticity-component equation, for example, t_z denotes the vortex tilting term in the ω_z equation computed as $\omega_x \partial w/\partial x + \omega_y \partial w/\partial y$. Similarly, in row 4 of Fig. 16, the diffusion term (d_x, d_y, d_z) is shown for each vorticity-component equation. The absolute value of each term in the vorticity equation is taken before computing the area integral. This allows estimation of their relative importance; the sign does not matter for this analysis. In **SL-UN**, the enstrophy components are limited to

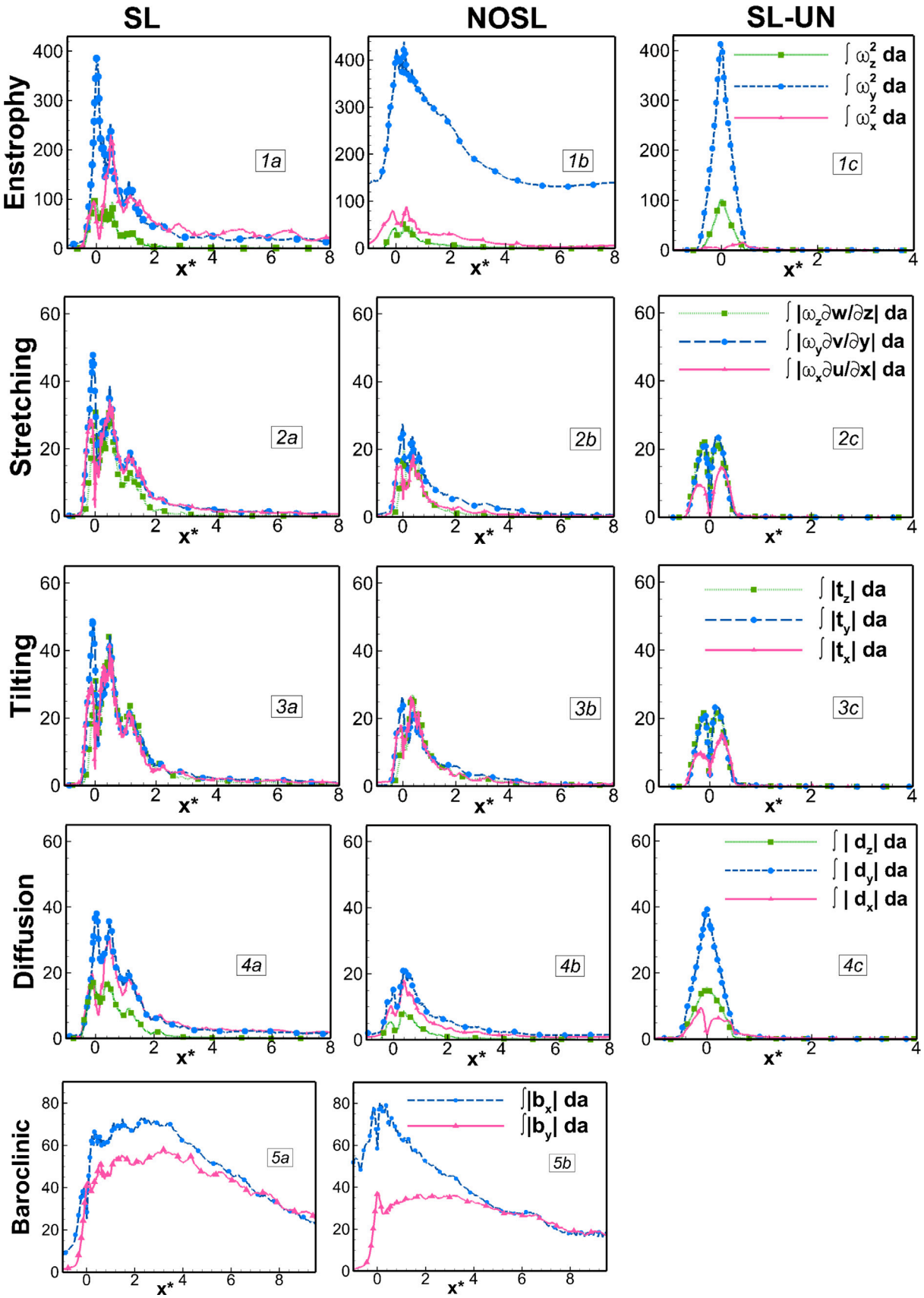

Fig. 16. Streamwise variation of $y-z$ plane-integrated vorticity (normalized by U_0^2) and vorticity budget terms represented in Eq. (8) (also normalized by U_0^2) at $t^* = 101$. Columns are (a) **SL**, (b) **NOSL**, and (c) **SL – UN**. Row 1 (top) shows the three components of squared vorticity (enstrophy). Row 2 shows the vortex stretching term, row 3 the vortex tilting term, row 4 the lumped diffusion term, and row 5 the baroclinic torque. In each figure of rows 2–5, terms in the ω_x, ω_y and ω_z equations are represented by green, blue and pink lines, respectively.

the obstacle with negligible values in the lee. Fluid can flow over the obstacle since stratification, which diverts oncoming fluid sideways around the obstacle, is absent. Hence, the spanwise vorticity (ω_y) is much larger than ω_z. The component, ω_x, is generated by tilting of ω_y and ω_z. Owing to viscous dissipation, the magnitude of each vorticity component decreases eventually.

The **SL** case is strikingly different from **SL-UN** although the same boundary conditions are in play. Each vorticity component increases in magnitude from its upstream zero value as the fluid flows past the obstacle. Fig. 16(1a) shows that there is significant enstrophy in both horizontal components, not just ω_y. Baroclinic torque (absent in **SL-UN**) is a source of both horizontal components and, as shown by Fig. 16(5a), it exceeds other sources of vorticity. Note, that the range of the vertical axis is larger for row 5 (baroclinic torque), relative to the rows showing the other sources. The vortex tilting term (t_z) and vortex stretching term ($\omega_z \partial w/\partial z$) in rows 3 and 2 of Fig. 16(a), respectively, are also substantial. Thus, the simulations demonstrate that baroclinic torque produces horizontal vorticity which is tilted and stretched to give ω_z, in accord with the lee-vortex mechanism proposed by Smolarkiewicz and Rotunno (1988). Vortex tilting reduces in magnitude with increasing downstream distance, which lowers the magnitude of ω_z relative to the other components as shown in Fig. 16(1a). Furthermore, the vortex tilt/stretch terms are isotropic with no directional preference for any particular component suggesting that these terms are operative at smaller scales of motion.

Baroclinic torque generated by density anomalies in the horizontal is also dominant in **NOSL** shown in Fig. 16(5b). However, unlike **SL**, the magnitude of ω_y far exceeds the other components as seen in Fig. 16 (1b). The reason is that the bottom boundary layer, which injects spanwise vorticity into the flow, persists over the entire streamwise extent, while the wake vorticity, which is the primary source of the other vorticity components, is dissipated by viscosity.

5. Summary and discussion

Both no-slip and slip BCs have been employed in past studies of stratified flow past an isolated obstacle. No-slip is the physically correct BC. However, when the computational grid is too coarse to resolve the physical boundary layer, application of the no-slip BC results in an incorrect numerical boundary layer. As an alternative, geophysical wakes at high Reynolds number have been simulated with a slip BC or by the imposition of a drag law which can be viewed as a partial-slip boundary condition. With the goal of clarifying the role of BC type, we conduct simulations with no-slip (**NOSL**) and slip (**SL**) BCs of flow past a conical obstacle (height h and bottom diameter D) in a uniformly stratified background. The selected problem has topographic Froude number of $Fr_h = U_0/Nh = 0.2$, and the Reynolds number of $Re_D = U_0 D/\nu = 15{,}000$ is moderate so that LES with high resolution of the boundary layer and wake turbulence is possible. Two additional cases are also simulated: A hybrid (**Hybrid**) case with no slip on the obstacle and slip at the flat bottom, and a drag law case (**DL**) wherein a quadratic drag law is imposed on the boundaries. Another important goal is to assess the role of baroclinicity in the observed vortex dynamics.

The stratified flow at $Fr_h = 0.2$ exhibits flow blocking upstream of the obstacle, streamlines that are diverted to go around rather than over the obstacle, an accelerated downslope jet, flow separation followed by recirculation, a lee wave, and wake vortices with organized ω_z in the lee. Many of these flow features are substantially altered by the type of BC. Notably, the lee vortices in **NOSL** take the form of an attached counter-rotating vortex pair with little unsteadiness in most of the recirculation region behind the body while, in **SL**, **DL** and **Hybrid**, counter-rotating vortices are shed off the body to form a Kármán vortex street. **SL**, **DL** and **Hybrid** exhibit lateral flapping of the wake which periodically transports fluid with higher streamwise momentum to the centerline and, consequently, the mean value of centerline defect velocity decreases substantially faster in the near wake relative to **NOSL**. At the selected $Re_D = 15{,}000$, bottom friction evidently exerts a strong constraint on the wake that reduces unsteadiness near the body in **NOSL**. It is only further downstream (x/D of this location increases with increasing depth) that the wake develops a sinuous barotropic instability.

The lee wake vortices show vertical variability in size. Independent of the BC, their horizontal size is proportional to the local diameter ($d(z)$) of the conical obstacle. The frequency of the vortex shedding that occurs in **SL**, **DL** and **Hybrid** does not vary with vertical location in the simulated cases. Spectra of streamwise (u) and lateral velocity (v) in the near-wake region of **SL** show discrete peaks at the vortex shedding mode, quantified as $St = f_s D/U \approx 0.24$. Although there is no discrete peak in the near-wake region of **NOSL**, farther downstream there is a peak in the v-spectrum at $St = f_s D/U \approx 0.5$ which is visually apparent as a sinuous instability of the wake in the horizontal plane.

The boundary layers on the flat and sloping bottom are resolved in **NOSL**. Therefore, a laboratory experiment conducted with the present obstacle geometry and $Re_D = 15{,}000$ and $Fr_h = 0.2$ would be expected to match the results of **NOSL** and not **SL**, **DL** or **Hybrid**. Indeed, for similar parameters of $Fr_h = 0.2$ and $Re_D = 13{,}700$, Hunt and Snyder (1980) report a quasi-steady recirculation zone containing an attached counter-rotating vortex pair with some irregular unsteadiness in the wake.

At the moderate Re of the present simulations, the boundary layer is laminar and it imposes a wall shear (τ_w) that is steady in time and has a drag coefficient of ≈ 0.02. Geophysical flows are at high Re with a turbulent boundary layer and a lower C_d, and a drag-law BC is often used to represent the boundary layer. The **DL** case in our study is undertaken with $C_D = 0.0025$, and gives results similar to **SL** and **Hybrid**. At high Re of geophysical wakes, **NOSL** is inappropriate because the viscous sublayer cannot be resolved and, therefore, a BC such as **DL** is appropriate.

Boundary-layer vorticity, curvature of the body and baroclinicity have been advanced as potential generators of the lee wake vortices. An unstratified simulation (**SL-UN**) is conducted to exclude baroclinicity from the generators of vorticity. In **SL-UN**, the flow remains attached over a much larger region, the wake that emerges is narrow, and large organized lee vortices are absent. Unstratified simulations with no-slip BC have not been conducted here, since there are prior laboratory experiments and simulations with the no-slip BC of the unstratified configuration. The prior studies show vortical structures different from the present lee vortices: a standing horseshoe vortex and periodic shedding of hairpin vortices at low Re_D (Acarlar and Smith, 1987) which changes to intermittent shedding of vortex patches at high Re_D (Garcia-Villalba et al., 2009). Therefore, we conclude that, independent of the choice of BC, unstratified flow does not demonstrate lee wake vortices of the type observed in geophysical wakes or in stratified-flow laboratory models of said wakes.

All components of the vorticity are prevalent in the flow as shown by the streamwise evolution of the squared magnitude (enstrophy) of each vorticity component. Owing to BL vorticity, the spanwise vorticity (ω_y) dominates the other two components upstream and downstream of the hill in the no-slip case. However, the increase in vorticity at the obstacle is similar among the different BCs. Instantaneous streamlines show opposite-signed vertical motion in the aft and lee as the fluid moves past the obstacle leading to the horizontal density gradients which are necessary for the baroclinic torque to be operative in the vorticity balance. Sources in the equation for each vorticity component are quantified and it is found that the baroclinic torque (operative only in the balances for horizontal vorticity components) is dominant, independent of the BC type. Vortex stretch and tilt are also substantial. The simulation result, namely, that horizontal vorticity is produced by

the baroclinic torque and tilted into the vertical, supports the lee-vortex mechanism proposed by Smolarkiewicz and Rotunno (1988).

Turbulence is quantified through the TKE. The lateral meanders of the wake in **SL** lead to high TKE in the wake. In **NOSL**, there is a zone of TKE that originates in the vertical shear layer between the fluid in the recirculation zone and the flow above associated with the lee wave and the separating downslope jet.

Declaration of competing interest

The authors declare that they have no known competing financial interests or personal relationships that could have appeared to influence the work reported in this paper.

CRediT authorship contribution statement

Pranav Puthan: Software, Visualization, Writing - original draft. **Masoud Jalali:** Software. **Jose Luis Ortiz-Tarin:** Software. **Karu Chongsiripinyo:** Software. **Geno Pawlak:** Conceptualization, Writing - review & editing. **Sutanu Sarkar:** Conceptualization, Writing - original draft, Writing - review & editing, Supervision.

Acknowledgments

We are grateful for the financial support provided by NSF, USA OCE-1737367. We would also like to thank the anonymous reviewers for their comments which helped to improve this manuscript.

References

Acarlar, M.S., Smith, C.R., 1987. A study of hairpin vortices in a laminar boundary layer. Part 1. Hairpin vortices generated by a hemisphere protuberance. J. Fluid Mech. 89, 1–41.

Baines, P.G., 1995. Topographic Effects in Stratified Flows. Cambridge University Press, 482.

Beckmann, A., Haidvogel, D.B., 1997. A numerical simulation of flow at Fieberling Guyot. J. Geophys. Res. 102, 5595–5613.

Buijsman, M., Klymak, J.M., Legg, S., Alford, M.H., Farmer, D., MacKinnon, J.M., Nash, J., Park, J.-H., Pickering, A., Simmons, H., 2014. Three-dimensional double-ridge internal tide resonance in Luzon Strait. J. Phys. Oceanogr. 44, 850–869.

Canals, M., Pawlak, G., MacCready, P., 2008. Tilted baroclinic tidal vortices. J. Phys. Oceanogr. 39, 333–350.

Carpenter, J.R., Smyth, W.D., 2019. Instability in Geophysical Flows. Cambridge University Press.

Chang, M.H., Jan, S., Liu, C., Cheng, Y., 2019. Observations of island wakes at high Rossby numbers: evolution of submesoscale vortices and free shear layers. J. Phys. Oceanogr. 49, 2997–3016.

Chongsiripinyo, K., Sarkar, S., Effect of stratification on the turbulent wake behind a sphere at Re = 10, 000, in: 10th International Symposium on Turbulence and Shear Flow Phenomena, TSFP10, 2017.

Chopra, K.P., Hubert, L.F., 1964. Kármán vortex-streets in earth's atmosphere. Nature 203, 1341–1343.

Coutis, P.F., Middleton, J.H., 2002. The physical and biological impact of a small island wake in the deep ocean. Deep Sea Res. I 49, 1341–1361.

Dairay, T., Obligado, M., Vassilicos, J., 2015. Non-equilibrium scaling laws in axisymmetric turbulent wakes. J. Fluid Mech. 781, 166–195.

Ding, L., Street, R.L., 2002. Numerical study of the wake structure behind a three-dimensional hill. J. Atmos. Sci. 60, 1678–1690.

Dong, C., McWilliams, J.C., Shchepetkin, A.F., 2007. Island wakes in deep water. J. Phys. Oceanograph. 37, 962–981.

Epifanio, C.C., Rotunno, R., 2005. The dynamics of orographic wake formation in flows with upstream blocking. J. Atmos. Sci. 62, 3127–3150.

Garabato, A.C.N., Williams, E.E.F., Spingys, C.P., Legg, S., Polzin, K.L., Forryan, A., Abrahamsen, E.P., Buckingham, C.E., Griffies, S.M., McPhil, S.D., Nicholls, K.W., Thomas, L.N., Meredith, M.P., 2019. Rapid mixing and exchange of deep-ocean waters in an abyssal boundary current. Proc. Natl. Acad. Sci. 116 (27), 13233–13238.

Garcia-Villalba, M., Li, N., Rodi, W., Leschziner, M.A., 2009. Large eddy simulation of separated flow over a three-dimensional axisymmetric hill. J. Fluid Mech. 627, 55–96.

Germano, M., Piomelli, U., Moin, P., Cabot, W.H., 1991. A dynamic subgrid-scale eddy viscosity model. Phys. Fluids A 3 (7), 1760–1765.

Grubisic, V., Sachsperger, J., Caldeira, R.M.A., 2015. Atmospheric wake of Madeira: First aerial observations and numerical simulations. J. Atmos. Sci. 72, 4755–4776.

Gula, J., Molemaker, M., McWilliams, J.C., 2015. Topographic vorticity generation, submesoscale instability and vortex street formation in the Gulf Stream. Geophys. Res. Lett. 42, 4054–4062.

Hasegawa, D., Yamazaki, H., Lueck, R.G., Seuront, L., 2004. How islands stir and fertilize the upper ocean. Geophys. Res. Lett. 31, L16303.

Hunt, J., Snyder, W., 1980. Experiments on stably and neutrally stratified flow over a model three-dimensional hill. J. Fluid Mech. 96, 671–704.

Kimura, S., Choo, H.S., Suginoto, T., 1994. Characteristics of the eddy caused by lzu-Oshima Island and the Kuroshio Branch Current in Sagami Bay, Japan. J. Oceanogrph. 50, 373–389.

Leal, L.G., 1989. Vorticity transport and wake structure for bluff bodies at finite reynolds number. Phys. Fluids A 1, 124–131.

Legendre, D., Luaga, E., Magnauet, J., 2009. Influence of slip on the dynamics of two-dimensional wakes. J. Fluid Mech. 633, 437–447.

Lesieur, M., 2008. Turbulence in Fluids. Springer.

Lilly, D.K., 1992. A proposed modification of the Germano subgrid-scale closure method. Phys. Fluids A 4 (3), 633–635.

Liu, C., Chang, M., 2018. Numerical studies of submesoscale island wakes in the Kuroshio. J. Geophys. Res. 123, 5669–5687.

MacKinnon, J.A., Alford, M.H., Voet, G., Zeiden, K., Johnston, T.M.S., Siegelman, M., Merrifield, S., Merrifield, M., 2019. Eddy wake generation from broadband currents near Palau. J. Geophys. Res. 124, 4891–4903.

Mashayek, A., Ferrari, R., Merrifield, S., Ledwell, J., Laurent, L.S., Garabato, A.N., 2017. Topographic enhancement of vertical turbulent mixing in the Southern Ocean. Nature Commun. 8:14197, 1–12.

Maslowe, S.A., 1991. Barotropic instability of the Bickley jet. J. Fluid Mech. 229, 417–426.

Meneveau, C., Lund, T.S., Cabot, W.H., 1996. A Lagrangian dynamic subgrid-scale model of turbulence. J. Fluid Mech. 19 (3), 353–385.

Molemaker, J., McWilliams, J.C., Dewar, W.K., 2015. Submesoscale instability and generation of mesoscale anticyclones near a separation of the California Undercurrent. J. Phys. Oceanograph. 45, 613–629.

Nikurashin, M., Ferrari, R., 2010. Radiation and dissipation of internal waves generated by geostrophic flows impinging on small-scale topography: Application to the Southern Ocean. J. Phys. Oceanogr. 40, 2025–2042.

Orlanski, I., 1976. A simple boundary condition for unbounded hyperbolic flows. J. Comput. Phys. 21, 251–269.

Pal, A., Sarkar, S., Posa, A., Balaras, E., 2016. Regeneration of turbulent fluctuations in low-Froude-number flow over a sphere at a Reynolds number of 3700. J. Fluid Mech. 804, R2,1–11.

Pal, A., Sarkar, S., Posa, A., Balaras, E., 2017. Direct numerical simulation of stratified flow past a sphere at a subcritical Reynolds number of 3700 and moderate Froude number. J. Fluid Mech. 826, 5–31.

Pawlak, G., MacCready, P., Edwards, K.A., McCabe, R., 2003. Observations on the evolution of tidal vorticity at a stratified deep water headland. Geophys. Res. Lett. 30, 2234.

Perfect, B., Kumar, N., Riley, J., 2018. Vortex structures in the wake of an idealized seamount in rotating, stratified flow. Geophys. Res. Lett. 9098–9105.

Perret, G., Dubos, T., Stegner, A., 2011. How large-scale and cyclogeostrophic barotropic instabilities favor the formation of anticyclonic vortices in the ocean.. J. Phys. Oceanogr. 41, 303–328.

Pinkel, R., Buijsman, M., Klymak, J.M., 2012. Breaking topographic lee waves in a tidal channel in Luzon Strait. Oceanography 25, 160–165.

Polzin, K.L., Garabato, A.C.N., Abrahamsen, E.P., Jullion, L., Meredith, M.P., 2014. Boundary mixing in Orkney Passage outflow. J. Geophys. Res. 119, 8627–8645.

Rapaka, N.R., Sarkar, S., 2016. An immersed boundary method for direct and large eddy simulation of stratified flows in complex geometry. J. Comput. Phys. 322, 511–534.

Rossi, T., Toivanen, J., 1999. A parallel fast direct solver for block tridiagnol systems with separable matrices of arbitary dimensions. SIAM J. Sci. Comput. 20(5), 1778–1793.

Rosso, I., Hogg, A.M., Kiss, A.E., Gayen, B., 2015. Topographic influence on submesoscale dynamics in the Southern Ocean. Geophys. Res. Lett. 42, 1139–1147.

Rotunno, R., Grubisic, V., Smolarkiewicz, P.K., 1998. Vorticity and potential vorticity in mountain wakes. J. Atmos. Sci. 56, 2796–2808.

Ruan, X., Thompson, A.F., Flexas, M.M., Sprintall, J.R., 2017. Contribution of topographically generated submesoscale turbulence to Southern Ocean overturning. Nat. Geosci. 10, 840–846.

Schar, C., Durran, D.R., 1996. Vortex formation and vortex shedding in continuously stratified flows past Isolated topography. J. Atmos. Sci. 54, 534–554.

Smith, R.B., 1989. Comment on "Low Froude number flow past three-dimensional obstacles. Part-I Baroclinically generated lee vortices". J. Atmos. Sci. 3611–3613.

Smith, R.B., Grubisic, V., 1993. Aerial observations of Hawaii's wake. J. Atmos. Sci. 50 (22), 3728–3750.

Smith, R.B., Smith, D.F., 1995. Pseudoinviscid wake formation by mountains in shallow water flow with a drifting vortex. J. Atmos. Sci. 52, 436–454.

Smolarkiewicz, P.K., Rotunno, R., 1988. Low Froude number flow past three-dimensional obstacles. Part-I baroclinically generated lee vortices. J. Atmos. Sci. 46 (8), 1154–1164.

Vosper, S.B., 2000. Three-dimensional numerical simulations of strongly stratified flow past conical orography. J. Atmos. Sci. 57, 3716–3739.

Vosper, S., Castro, I., Snyder, W., Mobbs, S., 1999. Experimental studies of strongly stratified flow past three-dimensional orography. J. Fluid Mech. 390, 223–249.

Warner, S.J., MacCready, P., 2014. The dynamics of pressure and form drag on a sloping headland: Internal waves versus eddies. J. Geophys. Res.: Oceans 119, 1554–1571.

Williamson, C.H.K., Brown, G.L., 1998. A series in $1/\sqrt{Re}$ to represent the Strouhal-Reynolds number relationship of the cylinder wake. J. Fluids Struct. 12, 1073–1085.

Yang, J., Balaras, E., 2006. An embedded-boundary formulation for large-eddy simulation of turbulent flows interacting with moving boundaries. J. Comput. Phys. 215, 12–40.

Zheng, Q., Lin, H., Meng, J., Hu, X., Song, Y.T., Zhang, Y., Li, C., 2008. Sub-mesoscale ocean vortex trains in the Luzon Strait. J. Geophys. Res. 113, 1–12.